MASTER THESIS

3D MORPHOMETRIC ANALYSIS OF WRIST BONE ANATOMY

Shreyas Vadhula Sainath

FACULTY OF ENGINEERING TECHNOLOGY
DEPARTMENT OF BIOMECHANICAL ENGINEERING

EXAMINATION COMMITTEE
Committee Chair- Prof. Dr. Ir. G. J. M. Tuijthof
Internal Member- Dr. -Ing. M. Asseln
External Member- Dr. A. Jalalian

DOCUMENT NUMBER
BE - <NUMBER>

UNIVERSITY OF TWENTE.

31-03-2025

TABLE OF CONTENTS

ABSTRACT

The focus of the thesis is to extract and analyze the 3D wrist bone shape to derive requirements for the Total Wrist Replacement (TWR) implant. The major challenges in designing these implants have been to account for the wide range of variation in wrist bones across the population. Designing a patient-specific implant is time-consuming and a simple gender-based design is not sufficient. To achieve successful implant function and longevity, it is important to understand these variations and design implants that are tailored to them. To address the issue of patient-specific and simple sex-based implant design, this thesis performs hierarchical clustering to understand the natural grouping in the population that can help in designing a wide range of implants.

This thesis uses the freely available Open-Source Carpal Database (OSCD). The features of the carpal bones, radius, ulna, and metacarpals were extracted using the Python scripting language and its libraries. The carpal surfaces were segmented using 2 approaches, vertex-normal and proximity-based, and Amberg's optimal step non-rigid iterative closest point (ANRICP) algorithm. The OSCD dataset was pre-processed to align with the anatomical coordinate system (ACS).

The carpal bone parameters showed a significant sexual dimorphism using independent t-test or Mann-Whitney U test ($p<0,05$). Males were generally larger than females with respect to carpal bone parameters. The segmented articular surfaces were significantly different when obtained by the 2 methods using paired Student t-test ($p<0,05$). Although the length, width, and surface area of the males were greater than those of the females with respect to the articular surfaces, the curvature values for the females were greater than those of the males, which could be the result of bone size. When it comes to reaming parameters, it was observed that women had a higher radial inclination (mean difference 0.29), carpal ratio (mean difference 0.07) and the curvature of proximal-PCR articular surface (mean difference 0.06) than men.

Clustering produced 15 groups when the features were selected based on their importance value. 14 groups were formed when only the PCR features and radial features were considered in the clustering based on ulnar variance (0-negative, 1-positive) and 11 groups were formed when the clustering was performed based on gender (0-female, 1-male). These results can be used to develop a series of designs for the implant.

1 INTRODUCTION

Implants used in Total Wrist Replacement (TWR) or wrist arthroplasty surgeries have evolved since their first design with the complex wrist joint modeled as a simple hinge joint by Swanson in 1967[1, 2], have seen continuous innovations and are currently in their 4th generation [2, 3]. The primary goal of the TWR is to preserve motion and relieve pain in the affected wrist [3, 4]. TWRs have progressed in their designs by focusing on mimicking the natural wrist structure and biomechanics of the wrist [2, 3, 5]. To mimic it, one must understand the anatomical, biomechanical overview of the wrist and the pathological conditions that affect the wrists that require TWR. The main challenge in designing wrist implants is to account for the wide range of anatomical variations in the wrist among individuals. Wrist bones, such as the radius, ulna and carpal bones, can vary significantly in size, shape and orientation. To ensure the success of wrist implant surgery, it is essential to analyze these variations and develop implants that can be tailored to the unique characteristics of each patient's wrist.

1.1 PATHOLOGICAL CONDITION (ARTHRITIS)

Arthritis, the condition that causes severe pain and movement limitations in the wrist, affects the patient's quality of life. Both rheumatoid [1, 3, 6, 7] and non-rheumatoid [1, 6] arthritis result in the need for TWR. These arthritic conditions can be degenerative, inflammatory, triggered by trauma, or failure of previous motion preserving surgery [1, 3, 6, 7]. They include conditions such as primary panacarpal osteoarthritis (PPOA) [1, 3, 6, 7], Kienböck's disease [1, 3], post-traumatic arthritis [1, 3], and scapho-lunate advanced collapse (SLAC) [1, 3]. Figure 1 illustrates radiographic images of SLAC and panacarpal arthritis.

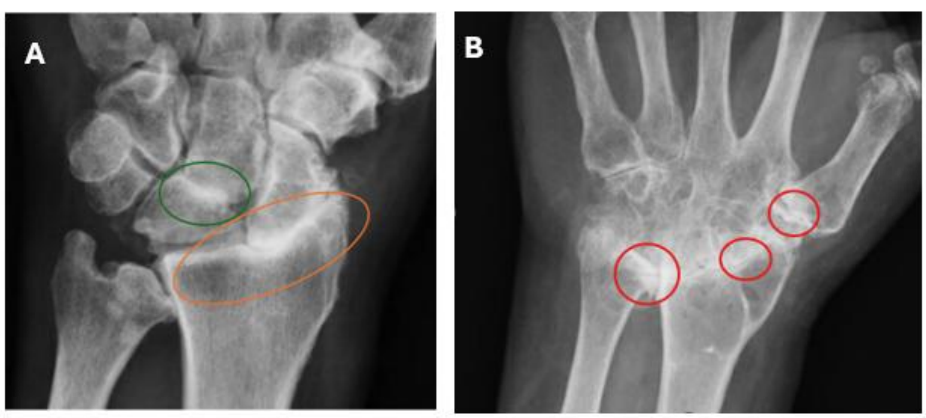

Figure 1: A: Stage III SLAC arthritis with markings showing collapsed regions, B: Panacarpal arthritis with marking showing some of the affected joint surfaces. Modified images referred from [8].

1.2 FUNCTIONAL ANATOMY OF WRIST

The human wrist is a bony skeletal structure consisting of carpal bones, which are supported at the distal end by the radius and ulna and articulate proximally with the metacarpals (MC). The carpus consists of 8 complex [9] and irregularly shaped bones [10] that also exhibit sexual dimorphism and present a higher degree of variation among ethnic groups [11-14]. Figure 2 shows the wrist bones in

3D and the grouping of these bones into proximal carpal (PCR) and distal carpal (DCR) rows based on the “row theory”[15]. This theory divides the carpals into PCR and DCR based on their biomechanical behavior and anatomy. The DCR act as a single unit connected by ligaments and move in response to the forces applied by the muscles of the forearm, whereas the PCR bones are not connected by any segment and exhibit independent motion [15]. The kinematics of the wrist is also impacted by the shape variations of the bones. In an example of lunate variations [16], wrists with type I lunates experienced a greater degree of motion during flexion-extension motion at the radiocarpal joint [17].

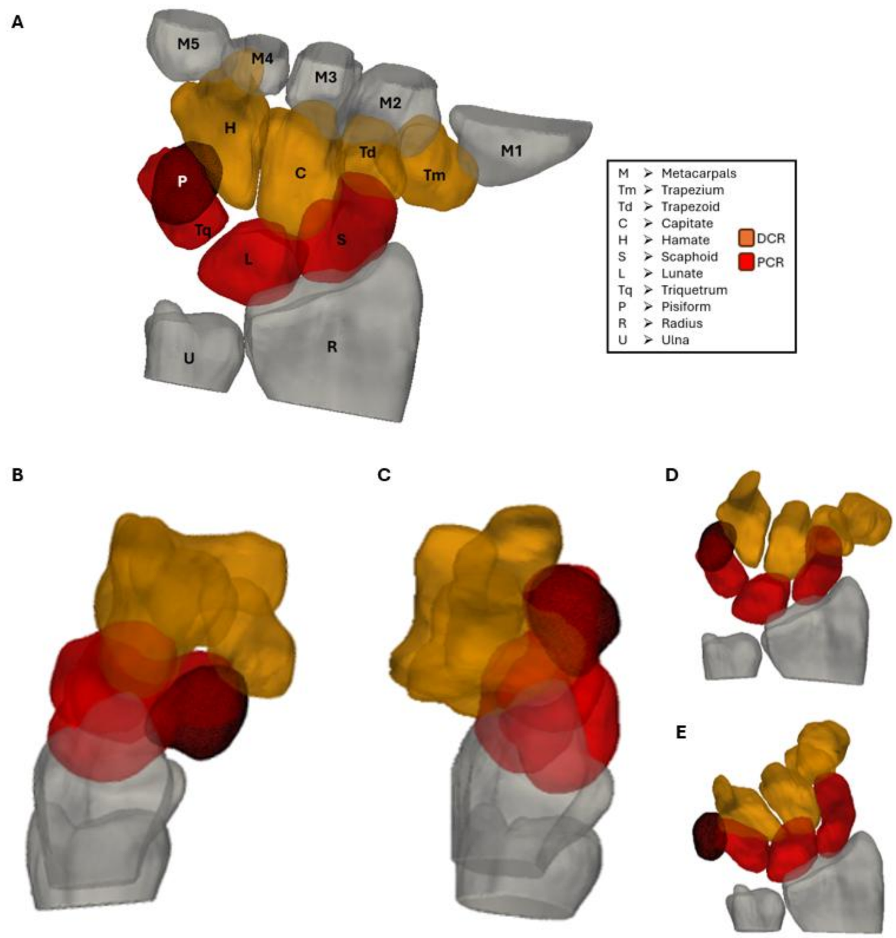

*Figure 2: **A** Palmar view of the wrist. Red: PCR namely: Scaphoid, Lunate, Triquetrum and Pisiform (dotted black structure). Orange: DCR namely: Trapezium, Trapezoid, Capitate, and Hamate (radial to ulnar). Articulating with the PCR are the Radius and Ulna bones proximally. **B** wrist in 60° flexion. **C** wrist in 60° extension. **D** wrist in 20° radial deviation. **E** wrist in 40° ulnar deviation. Motion data from the works Moore, D. C et al [9]*

The wrist, universally is estimated to have a 2 degree of freedom (DOF) with its motion defined along its orthogonal anatomical axes [15]. The joints of the wrist are classified into 4 categories namely distal radioulnar joint (DURJ), radiocarpal joint (RJ), midcarpal joint (MJ) and carpometacarpal joint (C-MCJ) [18] as shown in Figure 3. This combination allows the wrist to have a wide range of motion which includes flexion (75° - 85°), extension (70°-80°), radial (15°-20°) and ulnar (30°-40°) deviation as seen in Figure 3, and a degree of longitudinal rotation that can be performed individually or in combination [19].

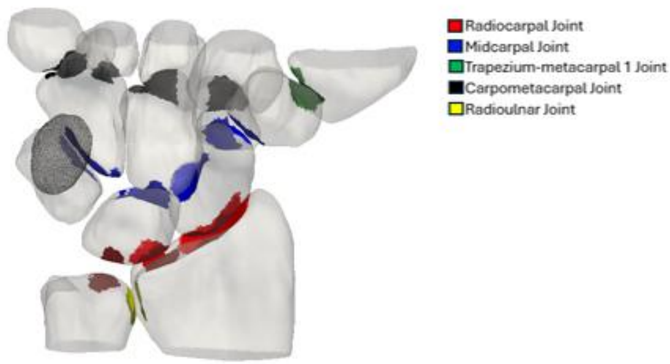

Figure 3: Wrist joints. Red: Radiocarpal joint (RJ), Blue: Midcarpal joint (MJ). Black: Carpometacarpal joint (C-MCJ). Yellow: Distal Radioulnar joint (DRUJ).

In the neutral position, the contact surface between the radius absorbed almost 80% of the force, while the ulna absorbed about 20% of the force that passed between the RJ. The force absorbed by the radius is transmitted by the scaphoid and lunate, which share 50% and 30%, respectively. The scapho-trapezial joint between the MJ transmits the highest 35%, with the least passing through the scapho-capitate joint, about 12% [20]. In the extended position, the forces transmitted to the radius through the scaphoid increased by 20% and decreased by 14% of the original force through the lunate. The forces on the scaphoid also showed a significant increase in the extended position of the wrist [21]. The anatomical variation of the wrist bones significantly affects the force and load distribution[22].

1.3 STATE-OF-THE-ART IMPLANT TECHNOLOGY

The first line of treatment for painful advanced wrist arthritis is arthrodesis (WA) [23-25], which stabilizes the carpal bones by restricting their natural motion this procedure reduces pain and provide comfort to patients [23-25]. Stabilization or fusion of the carpal bones is achieved by using implants (plates) fixed dorsally to the carpal bones or by intramedullary fixation implants [24]. With its drawbacks of restricting motion and not completely reducing the pain [24, 26], this remains one of the most widely used solutions (4 times [25]) due to its affordability and underlying conditions [25]. In order to maintain the functional ability of the wrist, wrist arthroplasty with functional wrist implants has been developed [3, 4]. Table 1 summarizes the 4 generations of functional wrist implants, while Table 2 summarizes the 4 generations of functional wrist implants, while.

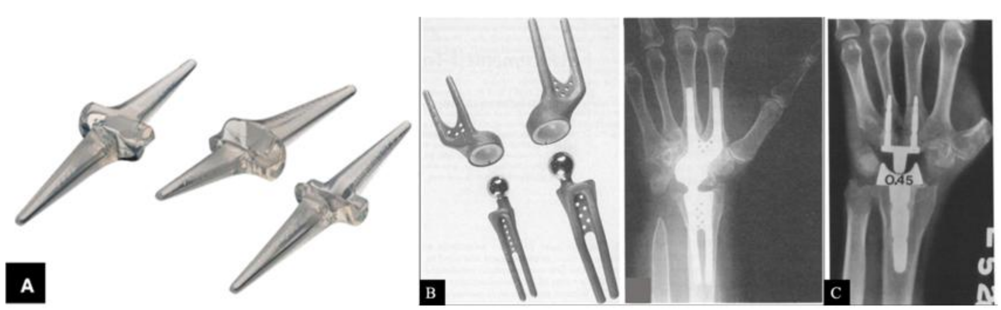

Figure 4: 1st [27] and 2nd gen wrist implants [2].

Figure 5: 3rd gen wrist implant [2].

Table 1: TWR Implant Generation [2].

Generation	Implant Name
First	Swanson Silicone Implant (Dow-Corning Corp., Midland, MI, USA)
Second	Meuli (Sulzer Orthopedics) Volz (Howmedica)
Third	Trispherical BIAX Total Wrist System (DePuy, Warsaw, IN, USA) Universal Total Wrist Implant (KMI, San Diego, CA, USA)
Fourth	Maestro (Biomet, Warsaw, IN, USA) Universal-2 (Integra LifeSciences, Plainsboro, NJ, USA) *Freedom (Integra LifeSciences, Plainsboro, NJ, USA) *ReMotion (Small Bone Innovations, Morrisville, PA, USA)

The first generation (Swanson Silicon Implant) is shown in Figure 4A, the second generation in (Meuli Implant Figure 4B, Volz Implant Figure 4C), and the third generation in Figure 5 (Trispherical Figure 5A, BIAX Total Wrist Implant Figure 5B, Universal Total Wrist Implant Figure 5C). As noted above, since the first application by Themistocles Gluck in Germany in 1890 [2], designers have sought to make the implant mimic the human wrist both anatomically and functionally. This evolution led to the development of today's state-of-the-art 4th generation implants. The design addresses complications such as loosening, stability, and MC stem cutouts, and focuses on reducing the use of cement for fixation [2].

The major issues faced with these 4th generation TWRs were the longevity of the carpal component due to the replacement of the multi-level articulation with a single radio-carpal articulation [3]. The common problems of loosening (17%), metallosis (8%), infection (8%), and stiffness (8%) [6] are still present in fourth generation TWRs. There is a need for better and more anatomically equivalent TWR's to be able to provide motion preservation treatment to patients with the above-mentioned pathologies.

As mentioned above, the next generation of Total Wrist Replacements (TWRs) under development aims to replicate the natural wrist structure and mimic its biomechanics. To achieve this, a thorough understanding of the anatomical features of the wrist bones is essential. Figure 7 shows some of the anatomical measurements required for the design of a TWR implant.

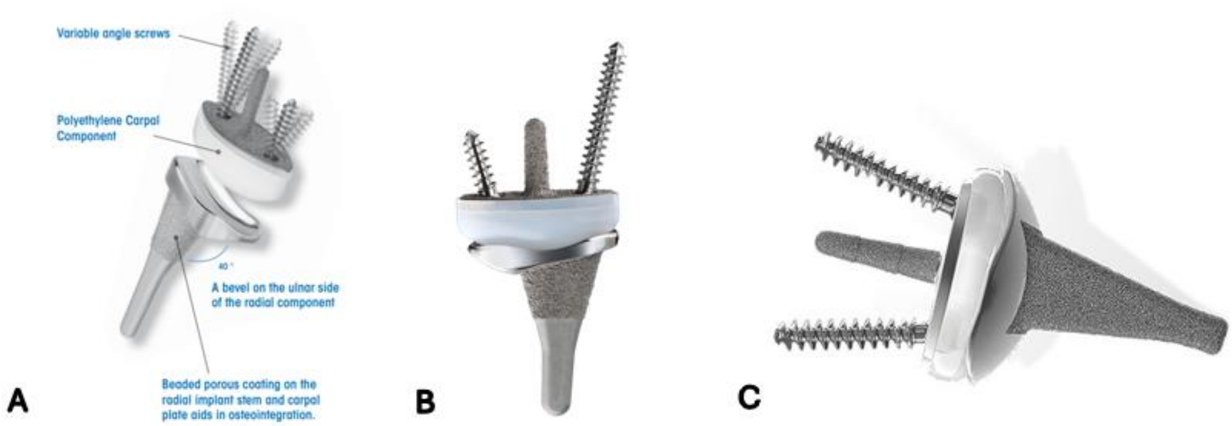

Figure 6: 4th Gen TWR's. A - Universal 2 Total Wrist Implant [28]. B - Freedom Total Wrist Implant [29]. C - ReMotion Total Wrist Implant [30]

Table 2: Material and Insertion point of the first 3 generations of TWR's [2].

Generation	**Material**	**Insertion point**
First	Made of Silicon elastomer	Intramedullary Radius, capitate, and 3^{rd} MC
Second	Titanium alloy or Cobalt chrome alloy and polyethylene	Intramedullary Radius, 2^{nd}, and 3^{rd} MC, with cement.
Third	Titanium or Cobalt chrome alloy or both in combination and ultra-high molecular weight polyethene (UHMWPE)	Intramedullary Radius, 2^{nd}, and 3^{rd} MC, with cement, and in case universal (3 insertions at the carpal end with one screw through capitate, 2^{nd} through trapezoid and 2^{nd} MC, and 3^{rd} through hamate.

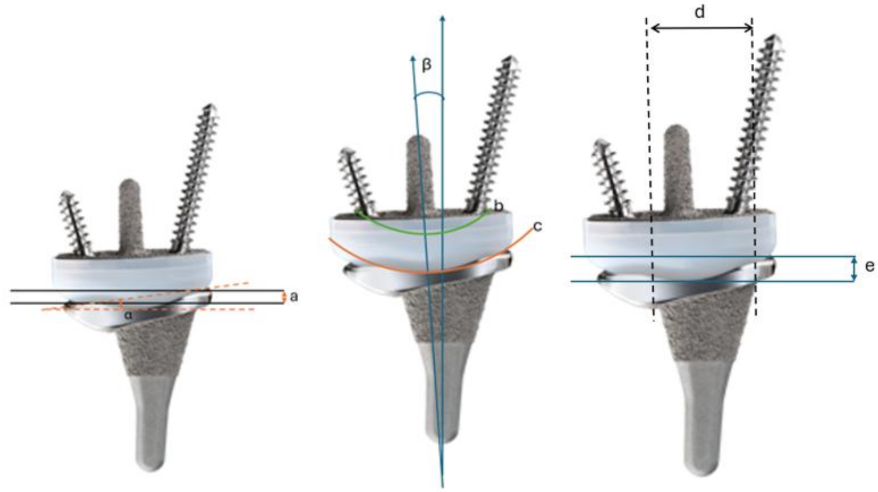

Figure 7: Some measurements that are used to design a wrist implant. a- radial height, α-radial inclination, β-radio-capitate angle, b-arc formed by PCR with DCR, c- radio-carpal arc, d- length of radio-carpal articulation surface, and e-height of radial styloid. Modified the image referred from [29].

1.4 AIM

Initially, anatomical measurements were performed on dry cadaveric bone specimens [11-14, 31-38] and on radiographs [11-14, 31, 33, 35, 37-40] using tools such as vernier calipers or digital calipers. The limitation of radiographic measurements is that they are sensitive to the position of the hand, with just a 15° rotation the length of the longest axis of the scaphoid changes by 8% [[41]. t has been observed that measurements taken with measuring tools such as calipers (macroscopic) are significantly different from those obtained with digital means [42]. The 3D computer-aided anthropometric measurements have been performed with the support of software's [43-47]. Some of these analyzed measurements and anatomical variations were extracted using atlas-based (ASM) or statistical shape models (SSM) using manually placed landmarks. The ASM and SSM manage to capture the shape variation in general, they then fail to capture precise measurements of individual bones [48]. hey also require accurate registration and segmentation, the errors produced in this step results in variation in the propagation of landmarks resulting in inaccurate morphometric assessments [49]. Atlas-based analysis is hampered by scalability issues that complicate the acquisition of specific measurements [50]. They are very time consuming and resource intensive as they depend on the initial training set provided to develop the model before applying it to the rest of the dataset [51].

This thesis focuses on the extraction and analysis of data derived from 3D bone meshes of the wrist. The goal is to perform statistical analysis to understand the variation of these features across populations and use the findings to inform future implant-specific design requirements. This task builds on previous work focused on the extraction and analysis of 2D data from wrist bones [52]. Here, we aim to advance the process by capturing features using 3D image processing libraries integrated with the Python programming language. It also analyzes the natural grouping of these anatomical features, which can then be used to aid in the design of TWR implants by identifying multiple shape variations based on aligned groups.

2 Material and Methods

2.1 Data Acquisition

The data used for this task was an open-source database called the “Open-Source Carpal Database” (OSCD) [9]. The database contained anatomical data on individual carpal bones from 90 healthy subjects including the age and gender demographics of the subjects. The OSCD contained data on a total of 120 wrists and their kinematics in 1.215 unique positions. The data sets are freely available online in the OSCD (https://simtk.org/projects/carpal-database, accessed May 20, 2024) [9]. This database was used in the previous work [52] and was therefore considered as the dataset for this thesis. The resolutions of the CT scans differed between the datasets, ranging from 0,2 × 0,2 mm to 0,4 × 0,4 mm in the transverse plane of the hand and 0,625 to 1 mm along the axis of the forearm [52]. Digital models of the outer cortical surface of the radius, ulna, eight carpal bones, and five metacarpals were obtained from neutral-posture CT images using Mimics v12-19 (Materialize, Leuven, Belgium) [9]. Neutral posture was defined as the posture in which the third metacarpal was aligned with the orientation of the two forearm bones. Cartilage information was not available from the CT images [9]. Our study included 117 wrist records (62 female and 55 male records) containing eight carpal bones, the radius, and the ulna. Three datasets were incomplete and excluded: the ulna is missing in datasets 62.641 (left) and 62.641 (right), and the trapezoid is missing in dataset 97.808 (right).

2.2 Computational Environment

The analysis was performed on Microsoft Visual Studios 2022 was used as the integrated development environment (IDE), with two different environments configured for scripting and executing the codes. The latest Python 3,12,4 was used to execute some of the code as it supports many of the newly added libraries, and an older version of Python version 3,8,20 in combination with Anaconda 3 was used to gain access to certain libraries that are not compatible with the newer version 3.12.4 version of Python. The hardware used was "Lenovo IdeaPad 5" with an "AMD Ryzen 7" processor, with "Windows 11" (64-bit) operating system. All the libraries used for the analysis with their version is showed in Table 3.

Table 3: Python libraries.

Python Library	Version
Trimesh	4,5,3
Pyvista	0,44,2
Sklearn	1,3,2
Pandas	2,0,3
Numpy	1,24,4
Scipy	1,10,1
Sksparse	0,4,14
Matplotlib	3,7,3
Seaborn	0,13,2

2.3 DATA PREPROCESSING

The data required some pre-processing as they were available in IV (OpenInventory) file format. They were converted to standard polygon mesh geometry (.stl) format using a custom program scripted in the previous work [52].The mesh was then transformed from its CT scanner coordinate system to the Anatomical Coordinate System as shown in Figure 8.

- X-Axis: The long axis of the radius shaft was selected as the primary reference direction with positive X-ais defined as running from the distal end to proximal end of the radius (natural alignment of the bone's shaft).
- Y-Axis: Defined as the axis perpendicular to the X-axis and was located at the center of the radial articular surface. The positive direction of the Y-axis was set to run from the ulnar side towards the radial side.
- Z-Axis: The Z-Axis was constructed using the cross product of the X and Y axes, resulting in a perpendicular direction to both. The positive direction of the Z-axis was defined based on the dorsal-to-palmar orientation.
- Origin: the origin of the coordinate system was defined as the projection of the intersection of X-axis and Y-axis onto the distal surface of the radius, serving as the anatomical reference point.[52].

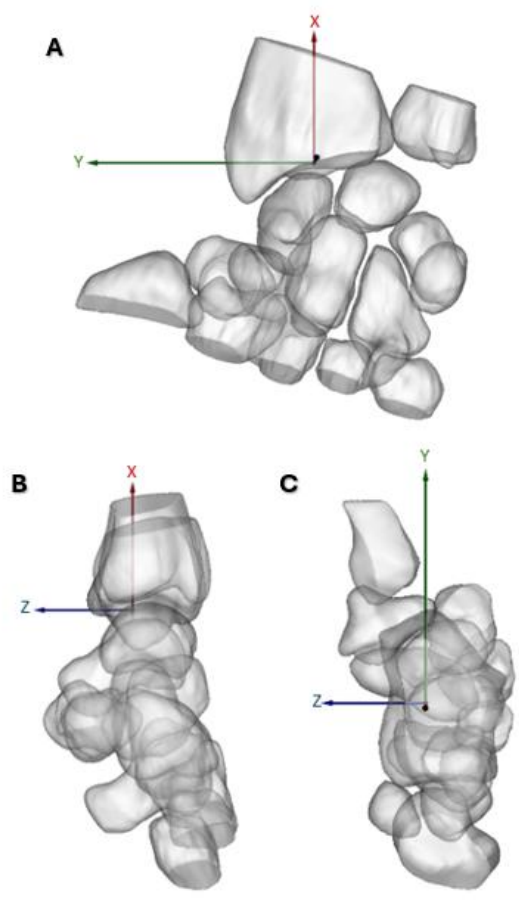

Figure 8: Mesh images of the wrist bone. A – frontal/palmar plane, B – Sagittal Plane, and C – Transverse Plane. The red line indicates X-Axis, green line indicates Y-Axis, and the blue indicates Z-Axis.

2.4 ARTICULAR SURFACE SEGMENTATION

The thesis also considered the articular surfaces of the wrist bones as its features. To segment these articular surfaces 3 approaches were considered, namely vertex normal and proximity-based segmentation and non-rigid iterative closest point (NRICP) based segmentation. This section briefs the 2 methods that are used for segmentation in this thesis. The flow chart of the code used here is presented in Appendix D.

The primary approach considered was to use an MRI image of the wrist to segment articulation surface, but due to unavailability of the required high-resolution images to get accurate segmentation this approach ended up being rejected. The use of the results from work of Dr. Magnús Kjartan Gíslason and Dr. David H. Nash, who had constructed a finite element model of the wrist which included the surface-to-surface contact setup between the wrist bones[53]. Since this was not available to be used on an opensource websites and were unable to acquire the same different approaches were considered.

2.4.1 Vertex Normal and Proximity-Based Segmentation

The articulation surfaces were segmented using proximity and vertex normal penetration between the two adjacent bones [54, 55]. Figure 9 shows the output of this approach, using the pyvista library with its "*find_closest_point*" function, which searches for points that are neighbors. Note that the point from which the search starts is part of the point cloud of the first bone (Lunate in Figure 9) and the search is performed on the point cloud of the second bone (Scaphoid in Figure 9). Once the search results are obtained, a distance threshold is added (here 4mm) and the area consisting of all the points that fall within this distance is segmented and used for the measurements. The limitation of this only the proximity-based method to segment articulation area depends on the distance threshold and this uncertainty was not desired to perform an anthropometric study and therefore was not used for further analysis. The previous works [54, 55] also did not use them directly but were interested in observing the relationship between the action of the wrist and that of the articular surface, and therefore this approach suited their study.

The vertex normal intersection between two bones, although gives the direct interaction region between the mesh surfaces [56] and ignores the involvement of soft tissues, that can then be segmented as an articulation surface and does not depend on any external threshold as input. Here, the vertex normal are calculated using the trimesh library function is then propagated to check if the normal intersects with the neighboring bone, this action is performed using the "*ray.intersects_any*" function of the trimesh library.

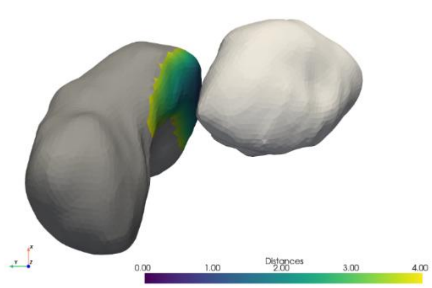

Figure 9: Proximity based articular surface segmentation (palmar view) of the scaphoid-lunate articulation surface.

This function assigns a Boolean value to the vertex depending on the intersection of it's normal with the neighboring mesh surface. Limitation of this approach is that the segmented articular surface, in case of hamate the hook region was considered to articulate with the capitate, which was not anatomically correct. This issue can be handled by using the method of Foumani M et al [57] and Teule E.H.S et al [58], where they initially start with selecting a larger surface (proximity range <=5mm) and then project the normal to intersect with the selected surface. Vertex that forms an angle in the range 180°±x° is segmented out as articulation surface. In this they aimed at measuring the dynamic distance between the joints. Here the a similar approach was used but the angle threshold of was not provided instead the complete surface that was intersected by the vertex normal were segmented as articular surface (Figure 10), based on the distance threshold of <=3mm to all the articular surface with exceptions to hamate-lunate (5mm) and lunate-ulna (10mm) as they are further apart from each other [34].

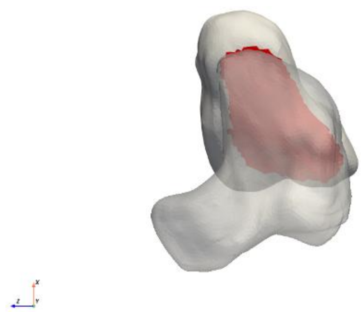

Figure 10: Capitate-hamate articulation surface (on capitate marked in red) in sagittal plane.

2.4.2 Non-Rigid Iterative Closest Point (NRICP) Based Segmentation

The last approach was to get the articulation surfaces segmented by a medical professional from University of Radboud on one dataset using MeshLab software (version 2023,12). These segmented articular surfaces were then propagated (template) and morphed on to the remaining datasets (target) and then segment articular surfaces [59]. Amberg's optimal step non-rigid ICP (ANRICP) algorithm [60] was used to perform the propagation and morphing. ANRICP algorithm had a lower registration error and a least spread in the RMSE vs probably density plot when compared to other NRICP approaches [60] and hence was used in this study. Figure 11 shows a template mesh of the capitate with all articulation surfaces identified by different colors.

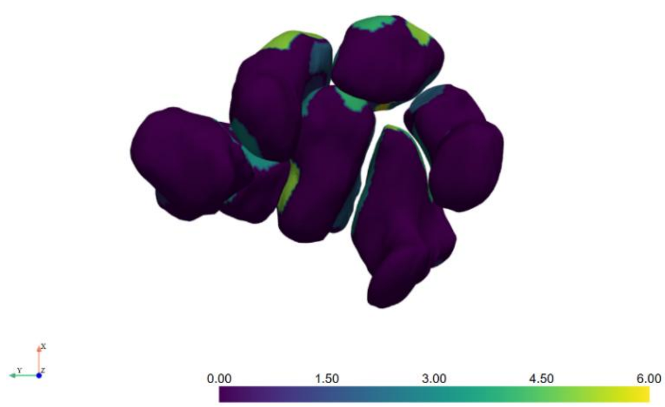

Figure 11: The figure illustrates the template carpal bones with their articulation surfaces marked with distinct colors (Palmar View).

This is now propagated to align with the centroid of the target mesh (both translational and rotational propagation occurs here) using the standard rigid ICP algorithm, then ANRICP is applied to morph the template bone over target bone. Once this step is complete, the KDTree algorithm is used to mark the closest points to each segmented region of the source on the target mesh. This is then masked with the same unique colors. Once this transfer is successfully completed as seen in Figure 12, the articulation surfaces are segmented and stored individually.

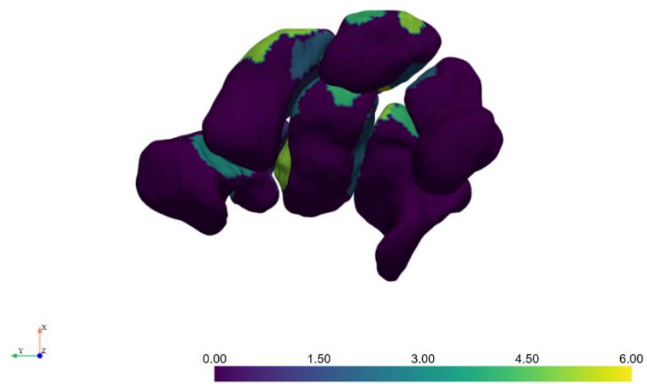

Figure 12: The figure illustrates the target carpal bones with their articulation surfaces marked with different colors (Palmar View).

2.5 Feature Selection and Measurements

As mentioned in the introduction, to being able to mimic the natural anatomy of the wrist into the design of the wrist arthroplasty implants the bone features are required to be extracted. This section lists all the bone morphometric parameters that were identified and whose measurements were extracted as features for this assignment. The features used in this thesis were selected from literature as shown in Figure 7. The features selected and the method used for their measurement are listed below. The flow chart of the code used here is presented in Appendix C.

2.5.1 Carpal Bone Parameters

2.5.1.1 Length and Width

Bone length and width are one of the most common features considered [11-14, 31-38]. The maximum distance between two points or the maximum variance observed in a bone (also referred to as the maximum length [11]) is defined as the length, and the maximum variance observed perpendicular to the length axis is defined as the breadth of the bone. In this study, the length and breadth of the metacarpals, radius and ulna are excluded because their imaging was limited by the scan range of the CT scanner along the x-direction. Most of the study measurements were obtained using calipers or digital calipers in combination with a profile using dry bone specimens or radiographs [11-14, 31, 33, 35, 37, 38].

As described by Hillman [32] the length of the carpal was measured by performing a search to find the farthest points among the vertices of the bone's mesh and was considered bone's longest axis. The length and breadth of the bone were obtained in the previous study using the bounding box principle [52]. The current work focuses on using Principal Component Analysis (PCA) to acquire these features from the carpal bone [36, 61]. The PCA provides 3 principal components (PC), of which the first 2 are of our interest along the maximum variance known as PC1, which is extracted as length, maximum variance along the bone perpendicular to PC1 known as PC2, which is extracted as breadth as shown in Figure 13.

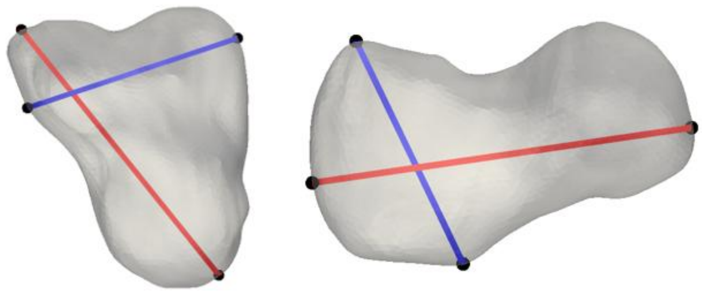

Figure 13: Plots of the wrist bone indicating the variance along PC1 (length) and PC2 (breadth). Lines with color red indicates length (PC1), and blue breadth (PC2). Left- Capitate Bone, Right - Scaphoid Bone.

2.5.1.2 3D Surface Area

The surface of these bone mesh is a collection of non-overlapping triangle connecting the vertices, the surface area of the carpal bones can be defined as the cumulative sum of the areas of these triangles. The library trimesh library offers a direct function known as "*area*" to calculate the surface area of the 3D mesh.

2.5.1.3 Volume

Volume is a very important feature of a bone, and it measured by water displacement method of the dry wrist bones [36, 62, 63]. The same is extracted using the trimesh libraries "*volume"* function.

2.5.1.4 Articular Surface Measurements

The surface area, length, width shown in Figure 14, mean and gaussian curvature of the segmented articular surface were extracted from the articular surfaces segmented as mentioned in 2.4 section.

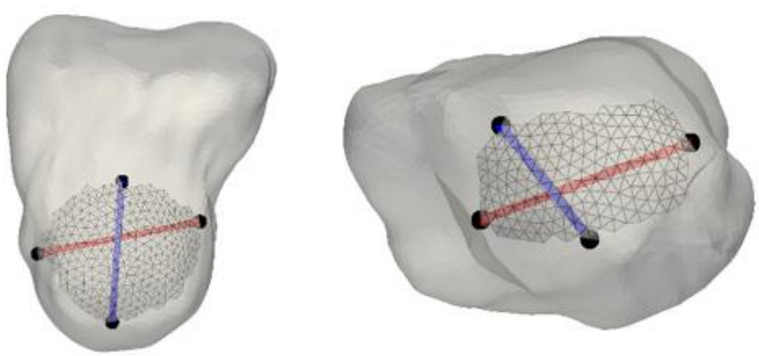

Figure 14: This figure illustrates the length (red line) and breadth (blue line) of the articulation surface of capitate with scaphoid (Left) and with lunate (right).

2.5.1.5 Proximal Carpal Curvatures

The importance of being able to mimic the curvature of the proximal row to ensures optimal contact between implant components, reducing wear and enhancing longevity [64]. The distal (with capitate, hamate, trapezium and trapezoid) and proximal (with radius) articular surfaces of the PCR are extracted using sphere fit method.

2.5.1.5.1 Distal Articulation Surface

The arc shape is defined by the distal articular surface of the proximal row of carpals. The proximal joint surface is defined by the vertices of the segmented joint meshes in the previous step, here the surfaces considered are the lunate-capitate joint surface, the scaphoid-capitate joint surface, and the triquetrum-hamate joint surface (points in black), and a mean sphere (red) is fitted to these points using the "least_squares" function of the "scipy.optimize" library, as seen in Figure 15.

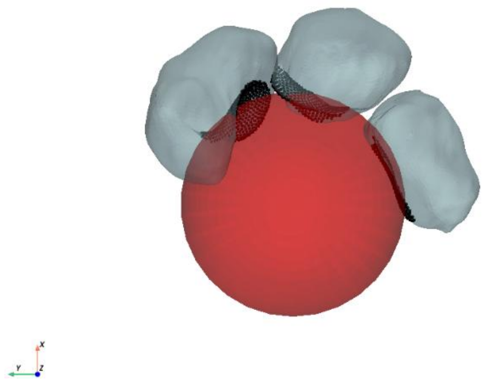

Figure 15: Average sphere fit for the distal articular surface of PCR ((Transverse view – in the direction of carpal to radius)

2.5.1.5.2 Proximal Articulation Surface

It follows the same procedure as of Figure 16, but the articulation surfaces considered here are the lunate-radius articulation surface, the lunate-ulna articulation surface, and the scaphoid-radius articulation surface. Since the triquetrum does not articulate with any bone on its proximal side, the surface is selected by using the vertex normal projects and filtering those vertices whose Normals are projected in the positive X, positive Z, and negative Y planes. This is illustrated in Figure 16 (points in black) and an average sphere is fitted to these points (green).

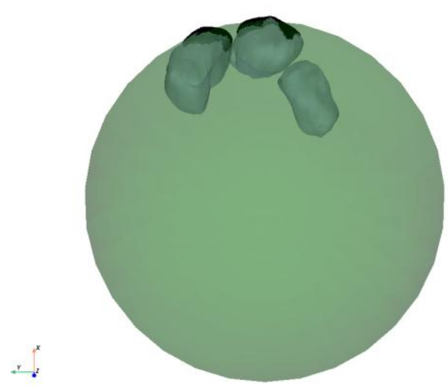

Figure 16: Average sphere fit for the proximal articular surface of PCR ((Transverse view – in the direction of radius to carpal)

2.5.2 Radial Parameters

2.5.2.1 Radial Height

It is defined as the distance between lines drawn perpendicular to the long axis, one of which passes through the radial styloid and the other through the most distal aspect of the ulnar articular surface

(2D) [40]. The same definition is used here as well, where the radial point is identified as the point that has the least X value to its coordinate (as in the RCS coordinate system) and the other point is the vertex that consists of the least X and maximum Y value to make the most distal aspect of the ulnar distal surface which also consists of its articular surface) as seen in Figure 17. Here, the distance is simply measured as the difference between the X values of the two points.

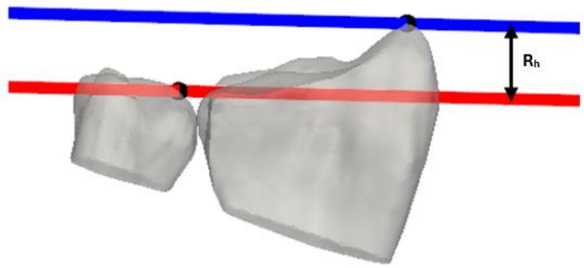

Figure 17: Lines drawn through the radial styloid (blue line) and through distal most aspect of ulna's distal surface (red line), perpendicular to long-axis. With R_h being the radial height measure.

2.5.2.2 Radial Inclination

It is the measure of the angle formed between the line joining the distal most point of the radius stolid tip and ulnar most point of the radial articulation surface and the line passing through the ulnar most point of the radial articulation surface perpendicular to the long axis (2D) [40, 65, 66]. As shown in Figure 18, the radial inclination defined here is like above, but the way the ulnar most point is identified is by finding the point that has the max value for the Y axis on the ulnar bone (RCS coordinate system) and using the "closest_point" function to find the point closest to this point on radius. Once this point is identified a radial search for its neighbors using "KDTree" is performed and the point with the least X value is considered as the point that is ulnar most point of the distal radius bone.

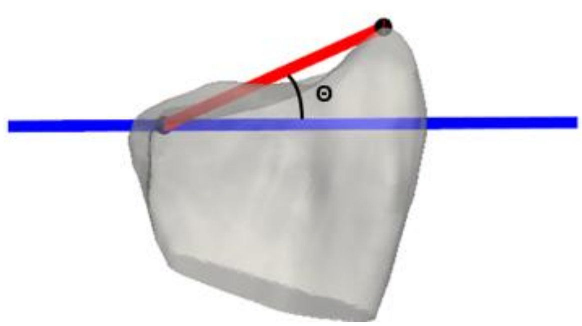

Figure 18: Indicating the line joining between the styloid tip and ulnar most point (Red) and the line passing through ulnar most point perpendicular to longest axis (Blue) whose angle (Θ) is considered as radial inclination.

2.5.2.3 Radio-Capitate Angle

It is defined as the angle formed between the longest axis of the capitellum and the radius [40]. The same definition is incorporated here by using PCA to identify the long axis of the capitate, the method is not incorporated on the radius as the entire radius is not imaged. For the radius, the long axis is determined as the line passing through the centroid along the X axis (RCS coordinate system), as shown in Figure 19.

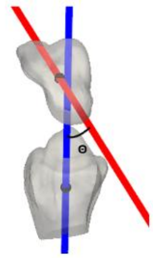

Figure 19: Illustrating the long axes of capitate (Red) and radius (Blue) to measure the radio-capitate angle (Θ).

2.5.2.4 Radius Articular Surfaces

Radio-scaphoid Figure 20 (Left) and radio-lunate Figure 20 (Right) articular surfaces were segmented using the first method explained in section 2.4. The length, width, and curvature measures of these articulation surfaces are extracted [66].

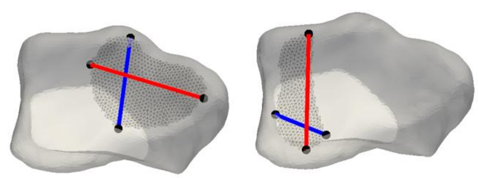

Figure 20: Segmented Radio-scaphoid articulation surface (Left) and Segmented Radio-lunate articulation surface (Right). The red line represents the length measure, and the blue line represents the width measure.

2.5.2.5 Radius Styloid Process Height

It is defined as the distance measured between the tip and the line perpendicular to the long axis at the medial edge of the distal end [67]. The definition remains almost the same, but the perpendicular line is defined here as the line drawn perpendicular to the long axis and passing through the point where the long axis passes through the distal articular surface of the radius, as shown in Figure 21.

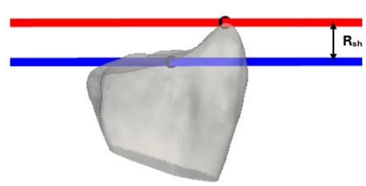

Figure 21: Illustrating the lines originating from points distal articular surface of radius (Blue) and tip of styloid process (Red) considered to measure the height of radius styloid process (R_{sh}).

2.5.3 Ulnar Parameters

2.5.3.1 Ulnar Variance

The method of perpendiculars was used to measure the ulnar variance. It is defined as the distance between the point that is the most distal part of the radius to the point that is the most distal on the ulnar cortical rim [68]. A similar approach is used to calculate the ulnar variance, here in 3D it is considered as the distance between the lines drawn perpendicular to the long axis of the radius (red), where line 1 passes through the ulnar most end of the distal articular surface of the radius (red) and line 2 passes through the radial most point of the distal ulnar articular surface (blue), as seen Figure 22.

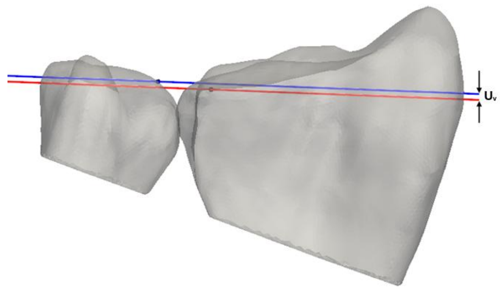

Figure 22: Illustrating the measure of Ulnar variance, in the above image the variance is positive (U_v).

2.5.3.2 Ulnar Axis Dome Angle

The dome angle is the angle between the long axis of the ulna and the line passing through the most distal point of the ulnar dome and the point where the ulnar dome meets the styloid [40]. Here, the definition is slightly modified to measure the angle between the long axis (red) and the line (blue) passing through the most distal point of the ulnar dome, which is the point that has the minimum X and maximum Y value, as shown Figure 23.

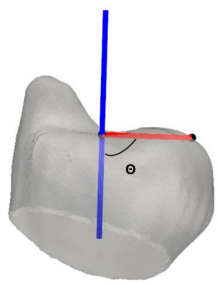

Figure 23: Illustrating the measure of ulnar dome angle (Θ).

2.5.3.3 Ulnar Styloid Process Height

The length of the ulnar styloid process is defined as the distance from the base to the tip of the process [69, 70]. The definition used here is like the radial styloid process height, where the styloid process tip is defined as the point with the lowest x-value and the base is the point where the long axis intersects the distal articular surface of the ulna, as shown in Figure 24.

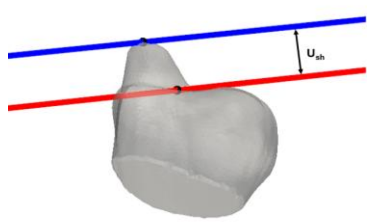

Figure 24: Illustrating the lines whose distance along X axis is measured as ulnar styloid height (U_{sh}).

2.5.4 Carpal Height Ratio

The carpal ratio is defined in the literature as the carpal height (L2) divided by the length of the capitate (L1) [39]. The carpal height is defined as the distance between the base of the third MC and the distal cortical margin of the radius along the extension of the longitudinal axis of the third MC [39]. This was performed as a 2D image on radiographs as shown in Figure 25 (Left) and on cadavers. To obtain the same on a 3D mesh, the definition is slightly adjusted. The definition of the carpal ratio used here is the distance between the centroid of the articular surface of MC3 with the capitate and the most distal point of the radius of interest with the longest axis passing through the centroid, as shown in Figure 25 (Right). The definition was altered to address the issue in constructing the long axis for MC3 as the MCs were not fully imaged since they were limited by the CT scan area along the x-axis.

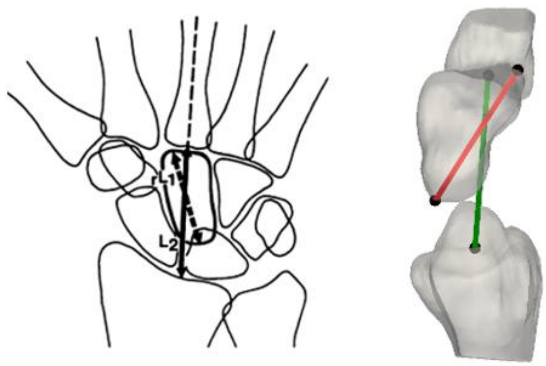

*Figure 25: The figure on the **left** pictorially describes the definition of the carpal height ratio [39], whereas the figure on the **right** describes the carpal height ration definition used for this assignment*

2.5.5 Palmar Tilt

It is defined as the angle between the line perpendicular to the long axis of the radius and the line joining the most distal points of the dorsal and ventral margins of the distal articular surface of the radius [40, 65, 66]. The same definition is used here, with the most distal point of the dorsal rim identified as the point with the minimum X value and maximum Z value, while that of the ventral rim is identified as the minimum X value and minimum Z value. This satisfies the definition because the radius is in the RCS coordinate system. The other line is simply a perpendicular line calculated by rotating the long axis along the Z axis. Figure 26 shows the lines (blue and green) used to measure the palmar title.

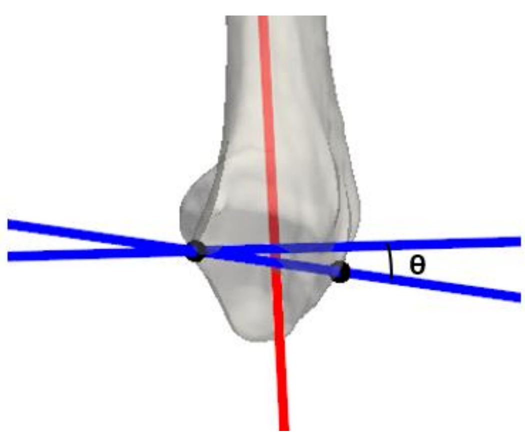

Figure 26: Illustrating the lines, Blue - line formed by joining the distal most point of ventral and dorsal rims, Blue - line perpendicular to long axis along Z axis, and red line shows the radius long-axis.

2.6 STATISTICAL METHODS

The data were cleaned to remove all NaN values depending on the type of analysis. For descriptive analysis, mean and standard deviation (SD), only the cells containing these NaN values were deleted, since the analyses were performed on individual columns, whereas for grouping, since there were dependencies between columns, the entire row of data was deleted before analysis. The NaN values were present in the extracted values for features related to articulation surfaces segmented using the first approach. This is either because the vertex normal intersection was not found or because the bones are further away from the set proximity threshold. The features with NaN values were mainly the hamate-lunate articulating surface segments and the lunate-ulna articulating surface segments. The gender variable was assigned with values 0 for female and 1 for male, whereas for ulnar variance variable 0 for negative variance and 1 for positive variance for analysis.

The mean and SD of the obtained values were calculated and compared to identify the variation among the carpal bones. The Python libraries such as Seaborn, Pandas, Matplotlib and Sklearn were used to perform statistical analysis. In order to evaluate the statistical difference between the male and female parameters, the data were first tested for normality using the Shapiro-Wilk test and homogeneity of variance using the Levene's test with a p-value of 0.05 as the threshold. Based on these tests, the difference was evaluated by either t-test or Mann-Whitney U test. A paired t-test was performed on the articular surface measurements obtained using the above methods to observe their significance, this method was considered because the comparison was between variables whose values were extracted using two different approaches. A p-value greater than 0.05 was considered the threshold for significance. Box plots were created to analyze the variation of the measure between male and female bones. Values were scaled using Sklearn's built-in "StandardScaler" function prior to analysis.

To understand the natural grouping present in the population (data set), Ward's Hierarchical Clustering was applied [71]. A dendrogram was plotted for the features, which is a tree-like structure that illustrates how the data points are grouped according to their similarity based on a certain distance metric. The dendrogram is divided into (from bottom to top) leaves, branches, and root. The leaves are the individual data points (sample index), the branches are the points that are close to each other that are grouped into smaller clusters, and the root is the final cluster that consists of all the data points. The grouping was performed at 20% of the maximum linkage distance of the dendrogram obtained from the hierarchical tree, and the importance values were calculated for each feature using the DecisionTreeClassifier function. The decision tree function assigns an importance value to the features based on their influence on the splitting and clustering of the data points.

3 RESULTS

3.1 BONE PARAMETERS

Table 4 shows the statistical measures that provide an overview of the variability in the length, width, area, and volume measures of the dataset. It is observed that the scaphoid bone has the highest variation along PC1 (length), followed by capitate, hamate, lunate, trapezoid, triquetrum, trapezium, and pisiform. When it comes to variation along PC2 (width), it is observed that Hamate has the highest variation followed by Capitate, Lunate, Scaphoid, Trapezium, Trapezoid, Triquetrum and Pisiform. Further, the data shows that there is a substantial variation in surface area and volume measures among the population as represented by them having large SDs'. It was also observed that these measures significantly varied between the two genders through independent t-Test or Mann-Whitney U Test ($p<0,05$) used depending on normality and homogeneity of the variance of individual variables. Figure 27 and Figure 28 show that there is a difference between the mean values of length and width for the male and female bones.

Table 4: The mean and SD of the datasets.

Bone	Parameters	Mean	SD	Bone	Parameters	Mean	SD
Capitate	Length(mm)	26,74	2,28	**Trapezoid**	Length(mm)	19,34	1,81
	Breadth(mm)	20,33	2,09		Breadth(mm)	15,09	1,73
	Surface Area(mm^2)	1221,41	205,04		Surface Area(mm^2)	650,03	118,89
	Volume(mm^3)	3106,27	729,29		Volume(mm^3)	1251,21	331,22
Hamate	Length(mm)	26,06	2,16	**Scaphoid**	Length(mm)	26,95	2,99
	Breadth(mm)	22,05	1,90		Breadth(mm)	17,48	2,23
	Surface Area(mm^2)	1129,50	184,94		Surface Area(mm^2)	1042,99	200,90
	Volume(mm^3)	2498,98	590,29		Volume(mm^3)	2345,87	649,51
Triquetrum	Length(mm)	19,31	1,85	**Lunate**	Length(mm)	19,90	2,30
	Breadth(mm)	14,23	1,25		Breadth(mm)	18,28	2,09
	Surface Area(mm^2)	666,32	120,14		Surface Area(mm^2)	804,83	170,39
	Volume(mm^3)	1340,74	349,66		Volume(mm^3)	1756,53	551,67
Trapezium	Length(mm)	23,73	2,34	**Pisiform**	Length(mm)	14,42	1,45
	Breadth(mm)	16,91	1,89		Breadth(mm)	11,48	1,35
	Surface Area(mm^2)	888,95	168,57		Surface Area(mm^2)	407,21	77,84
	Volume(mm^3)	1936,61	520,45		Volume(mm^3)	698,71	196,31

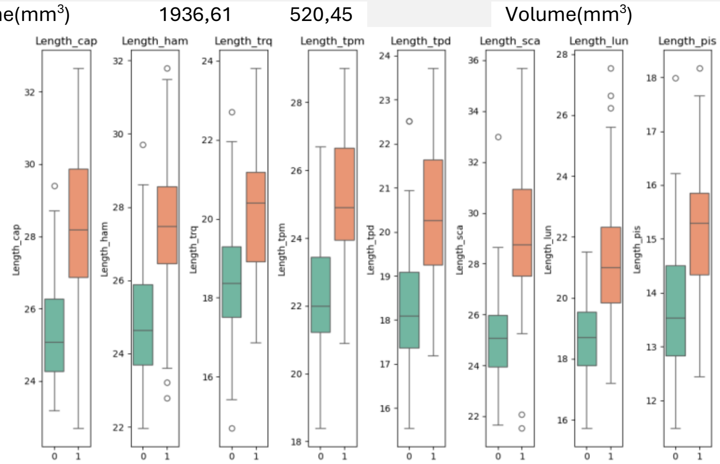

Figure 27: Boxplot comparing the length of the bone between male (1) and females (0).

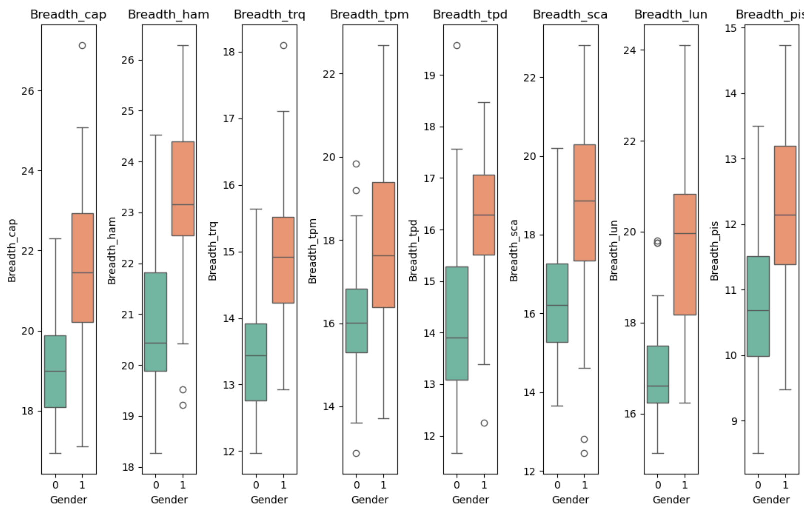

Figure 28: Boxplot comparing the breadth of the bone between male (1) and females (0).

3.2 ARTICULAR SURFACE PARAMETERS

As shown in Table 5, a simple comparison of the mean and standard deviation between the two approaches suggests that both approaches give similar results, with only the surface area showing a large difference. To obtain statistical significance, a paired Student's T-test (p <0,05) was performed, and it was observed that the measurements were significantly different with p-values close to 0 and higher t-values. It also future shows that the surface area of the trapezoid with scaphoid and lunate with triquetrum produced measures that are least significant, indicating that both approaches yield similar measures for these parameters (Surface_Area_tpd_sca and Surface_Area_lun_trq) as seen in Table 6. The full table is included in Appendix A (A1 and A2).

Table 5: Articular surface measures obtained using different approaches (the complete table can be seen in Appendix A (A1 and A2).

Bone Name	Articular Surface	Parameter	Mean	SD	Bone Name	Articular Surface	Parameter	Mean	SD
Capitate (Proximity and Normal Approach)	Lunate	Length(mm)	11,95	1,39	Capitate (NRICP Approach)	Lunate	Length(mm)	9,75	0,82
		Breadth(mm)	9,00	1,08			Breadth(mm)	6,68	0,65
		Surface_Area(mm²)	93,87	20,46			Surface_Area(mm²)	55,28	8,34
		Average_Mean_Curv(mm⁻¹)	0,15	0,02			Average_Mean_Curv(mm⁻¹)	0,14	0,02
		Average_Gaussian_Curv(mm⁻²)	5,95	0,62			Average_Gaussian_Curv(mm⁻²)	8,21	0,58
	Hamate	Length(mm)	20,37	1,90		Hamate	Length(mm)	21,13	1,83
		Breadth(mm)	14,01	1,39			Breadth(mm)	11,62	1,00
		Surface_Area(mm²)	190,48	33,27			Surface_Area(mm²)	176,85	29,16
		Average_Mean_Curv(mm⁻¹)	0,05	0,01			Average_Mean_Curv(mm⁻¹)	0,07	0,01
		Average_Gaussian_Curv(mm⁻²)	4,72	0,46			Average_Gaussian_Curv(mm⁻²)	5,64	0,37
	Scaphoid	Length(mm)	15,25	2,12		Scaphoid	Length(mm)	11,46	1,04
		Breadth(mm)	11,32	1,52			Breadth(mm)	9,36	0,73
		Surface_Area(mm²)	142,11	29,43			Surface_Area(mm²)	86,23	13,30
		Average_Mean_Curv(mm⁻¹)	0,12	0,02			Average_Mean_Curv(mm⁻¹)	0,13	0,02
		Average_Gaussian_Curv(mm⁻²)	5,21	0,67			Average_Gaussian_Curv(mm⁻²)	6,72	0,46
	Trapezoid	Length(mm)	14,93	1,93		Trapezoid	Length(mm)	14,26	1,41
		Breadth(mm)	11,35	1,82			Breadth(mm)	10,56	1,07
		Surface_Area(mm²)	100,61	24,81			Surface_Area(mm²)	113,58	21,28
		Average_Mean_Curv(mm⁻¹)	0,09	0,03			Average_Mean_Curv(mm⁻¹)	0,05	0,02
		Average_Gaussian_Curv(mm⁻²)	7,46	1,30			Average_Gaussian_Curv(mm⁻²)	6,70	0,55
	MC3	Length(mm)	15,53	1,66		MC3	Length(mm)	16,53	1,48
		Breadth(mm)	11,63	1,43			Breadth(mm)	10,09	1,06
		Surface_Area(mm²)	113,93	22,90			Surface_Area(mm²)	105,27	17,28
		Average_Mean_Curv(mm⁻¹)	0,09	0,01			Average_Mean_Curv(mm⁻¹)	0,10	0,02
		Average_Gaussian_Curv(mm⁻²)	6,19	0,59			Average_Gaussian_Curv(mm⁻²)	7,06	0,43

Table 6: The p-Values of the parameters that showed least significance between the values obtained.

Parametes	p-Values
Surface Area_lun_trq	0,64
Average Mean Curvature_lun_trq	0,47
Length_lun_uln	0,14
Average Gaussian Curvature_lun_ham	0,11
Length_ham_lun	0,53
Average Gaussian Curvature_ham_lun	0,30
Average Gaussian Curvature_sca_lun	0,33
Average Mean Curvature_sca_tpm	0,13
Breadth_sca_tpd	0,71
Length_tpd_cap	0,17
Average Mean Curvature_tpd_cap	0,49
Length_tpd_sca	0,36

Figure 29 and Appendix B show the box plots of the articular surface curvature measures. It is evident that the articular surface curvatures are higher in females compared to males.

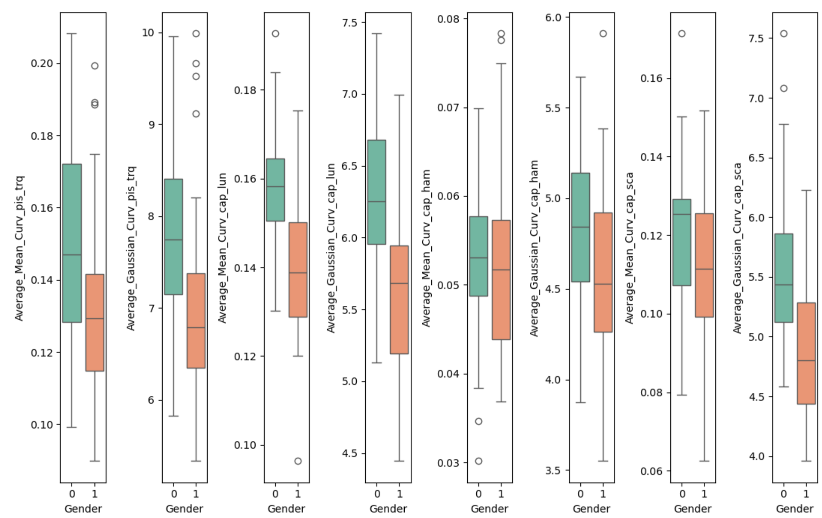

Figure 29: Boxplot comparing the articulation curvatures between male (1) and females (0).

3.3 Other Parameters

Table 7: Table A depicts the mean and standard variation values for the complete dataset and B depicts the same dataset grouped by gender. Table 7A shows the mean and standard deviation among the other features considered in this study. that radio-capitate angle and Capito-lunate angle have a higher spread, which is the result is how the angle is measured. Since these angle measurements depend on the long axis, which is considered along PC1 and show variation between data sets that directly affect the measured angle. When comparing between genders as shown in Table 7B, it is observed that females have a larger carpal ratio, which is a direct result due to larger bone in males, and females have slightly larger outer radius (PCR).

Table 7: Table A depicts the mean and standard variation values for the complete dataset and B depicts the same dataset grouped by gender.

A

Prameters	Mean	SD
r_internal (mm)	13,06	1,39
r_external (mm)	34,60	6,19
internal_relative_error	0,08	0,01
external_relative_error	0,02	0,00
Ulnar_Dome_angle (°)	85,58	9,56
ulnar_stlyloid_height (mm)	4,45	2,14
ulnar_var	0,24	0,43
palmar_tilt_angle (°)	19,19	5,33
Radius_styliod_length(mm)	7,04	1,44
Radio_Capitate_angle(°)	44,83	21,08
Radial_incline_angle(°)	22,90	3,95
Radial_height(mm)	11,61	2,84
carpal_ratio	0,61	0,40
capitate_lunate_angle(°)	81,60	26,30

B

Gender	Male		Female		Mean Difference (male-female)
	Mean	SD	Mean	SD	
r_internal(mm)	13,95	1,27	12,22	0,87	1,73
r_external(mm)	34,57	5,54	34,63	6,80	-0,06
Ulnar_Dome_angle(°)	87,55	9,65	83,74	9,18	3,80
ulnar_stlyloid_height(mm)	4,76	1,80	4,15	2,39	0,61
ulnar_var	0,16	0,37	0,32	0,47	-0,16
palmar_tilt_angle(°)	19,80	5,40	18,63	5,26	1,17
Radius_styliod_length(mm)	7,86	1,38	6,29	1,03	1,57
Radio_Capitate_angle(°)	47,51	21,22	42,33	20,81	5,18
Radial_incline_angle(°)	22,75	4,01	23,04	3,92	-0,29
Radial_height(mm)	12,57	2,46	10,71	2,89	1,86
carpal_ratio	0,57	0,38	0,65	0,43	-0,07
capitate_lunate_angle(°)	82,34	29,56	80,91	23,08	1,43

3.4 DATA GROUPING

Hierarchical clustering produced eight groups at 20% of the maximum linkage distance from the dendrogram as shown in Figure 30. When calculating the "importance" for the feature, it was seen that the clustering was based on the volume of the bones, the surface area, the length and width of the articular surfaces, and the carpal ratio, which were the top ten.

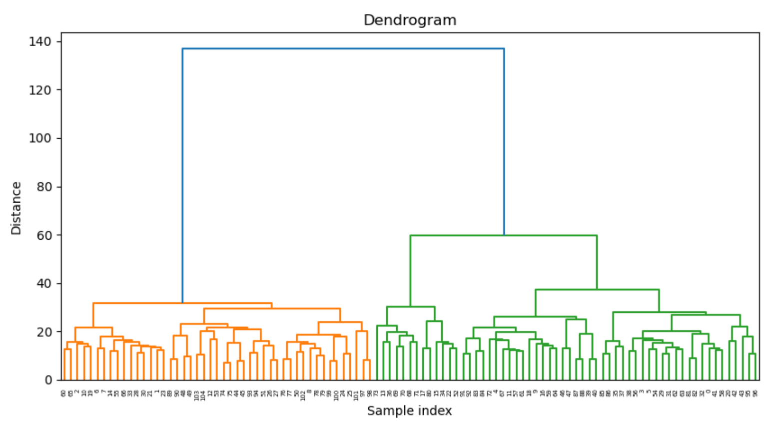

Figure 30:Dendrogram of all the measurements.

To make the grouping process more efficient, the data were separated into different sets, namely data with values for the parameters volume, length, width, curvature, surface area, and other measurements. Hierarchical clustering was performed on these datasets and grouped at 20% linkage distance. Only the parameter with the highest importance value from each group was selected for the volume, length, breadth, curvature and surface area datasets, and in other measurements parameters top 5 important parameters were selected. For the other measurement datasets, more parameters were selected because they produced the highest number of groups, as shown in Table 8. Figure 31 shows the dendrogram for the other measurement dataset and Table 8 shows how the number of groups and the order of importance change for the parameters based on the distance threshold. The 20% was chosen because it can be seen from Table 8 and all the dendrogram figures that higher variation and complexity within the dataset at lower levels, this is also to capture and preserve the natural structure of the data and allows us to reflect on its underlying diversity.

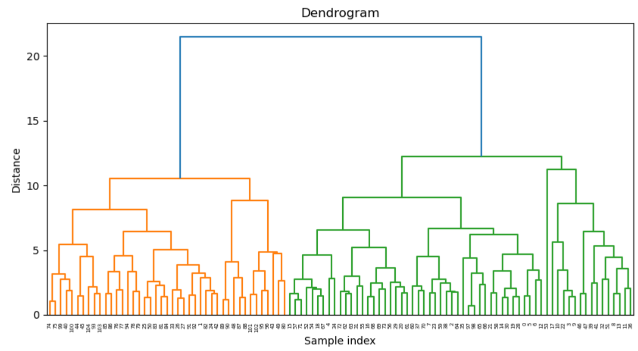

Figure 31: Dendrogram for other measurements.

Table 8: Difference in parameters considered for grouping depending on distance threshold.

% Linkage Distance	No. of Groups	Parameters (Top 5)
20	28	r_external Radio_Capitate_angle r_internal Radial_height Palmar_tilt_angle
40	8	Carpal_ratio Capitate_lunate_angle r_external Radial_height Radial_incline_angle
60	2	Carpal_ratio Radial_height Capitate_lunate_angle Palmar_tilt_angle Ulnar_Dome_angle

The following parameters were used for the analysis: r_external, Radio_Capitate_angle, r_internal, Radial_Height, Palmar_Tilt_angle, Volume_tpm, Breadth_tpm_tpd, Length_tpd_mc2, Average_Gaussian_Curv_sca_cap, and Surface_Area_tpd. The clustering produced the dendrogram shown in Figure 32. The clustering for the dataset considering only these parameters grouped them into 15 groups with the highest importance for the Radio-Capitate angle parameter.

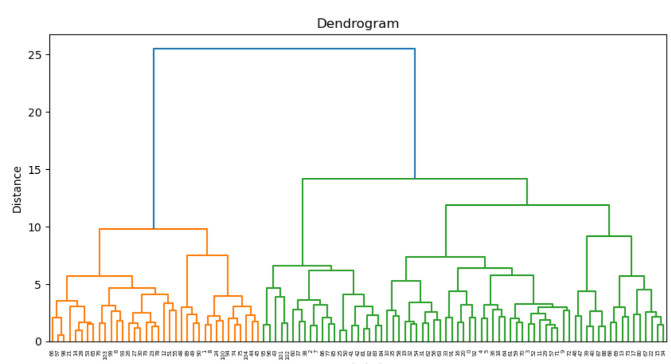

Figure 32: Dendrogram for the selected parameters.

On the other hand, while considering the parameters of the PCR carpals and the radius such as lunate and scaphoid bone and joint parameters, radial inclination, radial height, radial styloid height, and radial articular parameters with ulnar variance 14 groups were formed as shown in the dendrogram Figure 33A and the Table 9 gives and overview of the mean and SD values of these parameters while when the gender feature was considered 11 groups were formed as shown in Figure 33B and Table 10.

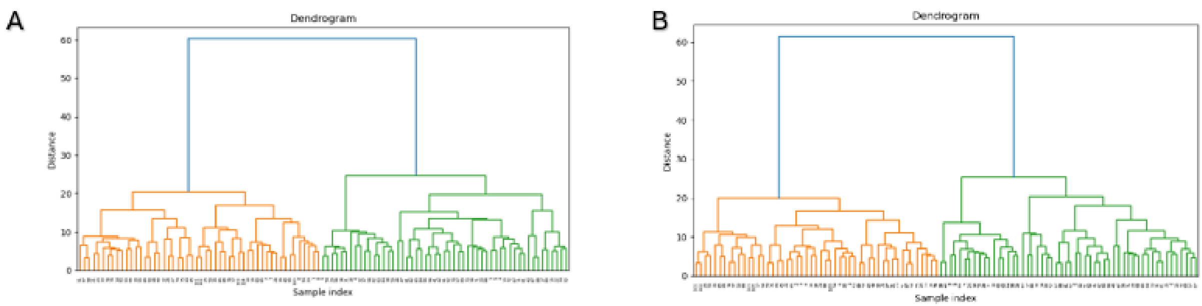

Figure 33: A- Clustering when ulnar_var was considered as a feature, and B- Clustering when gender was considered as a feature.

Table 9: Groups formed been ulnar_var was considered.

Cluster		1	2	3	4	5	6	7	8	9	10	11	12	13	14
r_external	mean	32,24	42,16	32,13	39,85	36,51	35,00	28,98	33,30	29,45	34,10	28,24	33,42	41,78	37,52
	std	4,69	5,07	3,95	6,02	5,36	0,15	2,52	4,36	1,65	5,31	3,23	4,19	7,87	2,32
Radio_Capitate_angle	mean	31,18	76,60	61,35	51,55	28,15	65,57	64,42	26,58	82,07	52,45	26,84	35,77	73,21	37,93
	std	10,44	3,87	18,48	18,50	11,76	7,40	4,77	13,86	0,36	17,26	6,67	17,41	8,19	12,84
carpal_ratio	mean	0,86	0,32	0,32	0,30	1,02	0,17	0,46	0,94	0,22	0,41	0,81	0,83	0,22	0,88
	std	0,43	0,06	0,24	0,15	0,18	0,05	0,35	0,27	0,02	0,35	0,20	0,19	0,05	0,39
Radius_styliod_length	mean	6,09	5,26	5,42	6,24	6,63	6,66	6,60	7,41	9,54	7,99	9,53	8,80	6,17	8,95
	std	0,66	0,60	1,12	0,66	0,66	0,41	0,55	0,92	0,06	0,75	0,60	0,89	0,38	0,78
Radial_incline_angle	mean	23,31	18,64	20,83	22,30	23,11	21,39	22,64	24,01	27,37	23,69	26,66	26,10	13,69	23,28
	std	2,32	1,72	4,23	3,76	1,46	1,77	3,03	2,83	0,61	2,96	1,38	0,78	0,81	3,41
r_internal	mean	11,83	14,00	12,07	11,76	12,77	15,44	12,96	12,99	16,89	13,00	13,39	14,36	14,91	15,08
	std	0,89	0,91	0,71	0,58	0,72	0,14	0,91	0,91	0,14	0,64	0,79	0,77	1,20	0,84
Radial_height	mean	10,96	9,52	7,97	10,53	11,49	10,16	8,44	13,14	11,68	12,52	14,83	14,21	9,02	15,36
	std	1,04	2,03	2,86	2,29	1,12	0,83	2,36	1,67	0,25	2,02	1,12	1,45	0,86	2,33
palmar_tilt_angle	mean	17,27	19,13	21,16	21,35	18,13	23,75	21,52	16,04	16,13	23,70	17,70	16,14	22,28	16,92
	std	5,26	3,36	3,75	6,20	5,12	1,02	7,28	4,90	4,77	2,87	2,91	4,14	5,94	5,13

Table 10: Groups formed with gender been considered.

Cluster		1	2	3	4	5	6	7	8	9	10	11
r_external	mean	38,84	33,71	32,45	42,16	31,96	35,00	32,80	40,24	35,34	29,45	30,68
	std	5,69	4,05	5,50	5,07	4,87	0,15	4,49	4,92	5,07	1,65	2,98
Radio_Capitate_angle	mean	43,79	75,23	47,09	76,60	32,87	65,57	26,84	42,04	58,20	82,07	35,56
	std	21,23	2,76	18,75	3,87	12,26	7,40	11,63	22,63	12,22	0,36	17,39
carpal_ratio	mean	0,51	0,21	0,74	0,32	0,72	0,17	0,93	0,76	0,34	0,22	0,78
	std	0,42	0,11	0,40	0,06	0,41	0,05	0,28	0,43	0,27	0,02	0,28
Radius_styliod_length	mean	6,23	4,59	6,58	5,26	6,05	6,66	7,68	8,51	7,39	9,54	9,03
	std	0,59	0,47	0,56	0,60	0,63	0,41	0,77	1,41	0,74	0,06	0,76
Radial_incline_angle	mean	22,59	17,65	22,82	18,64	24,00	21,39	24,62	21,86	20,71	27,37	26,13
	std	3,48	1,01	2,40	1,72	1,98	1,77	2,81	5,10	3,72	0,61	1,47
r_internal	mean	11,67	12,01	12,74	14,00	11,96	15,44	13,33	14,64	13,24	16,89	13,91
	std	0,61	0,90	0,76	0,91	0,83	0,14	0,92	1,10	1,20	0,14	0,86
Radial_height	mean	11,06	6,12	9,83	9,52	10,89	10,16	13,49	14,50	11,04	11,68	14,31
	std	2,21	0,92	2,23	2,03	1,47	0,83	1,72	3,10	1,66	0,25	1,40
palmar_tilt_angle	mean	20,03	23,27	18,96	19,13	18,20	23,75	16,66	17,08	22,65	16,13	18,58
	std	6,61	2,79	5,97	3,36	4,99	1,02	4,72	5,06	5,50	4,77	4,21

4 DISCUSSION

The primary objective of this thesis was to extract 3D features of the wrist bone to study and analyze their variations and natural groupings formed across populations. The long-term goal is to gather data that can be used to derive design requirements for the next generation of TWR implants. This analysis is being conducted considering the approach to designing TWRs by mimicking the natural structure and function of the wrist [2, 3, 5].

In this study, various anatomical parameters were extracted including carpal bone dimensions, radial and ulnar parameters. These measurements were obtained using the 3D image processing libraries of the Python scripting language. This method helped in direct measurements in 3D compared to traditional methods using 2D radiographs [11-14, 31, 33, 35, 37, 38] or direct measurements using cadavers [11-14, 31-38]. These automated measurements using a script helped to derive features from a larger sample size, providing a more comprehensive understanding of wrist bone variations. The rationale for using a 3D approach is that measurements obtained from 2D radiographs are highly sensitive to hand position [41]. With complex structures, such as wrist bones, using 3D assessments methods provides a more consistent and dependable results [72]. 3D measurements have a greater reproducibility and accuracy in reflecting the actual clinical scenario than through radiographs [73].

The study revealed considerable variability in the anatomical measurements of the wrist bones, with the scaphoid having the greatest length (PC1), followed by the capitate and hamate, while the hamate had the greatest width (PC2), followed by the capitate, lunate, and scaphoid. The Length measurements were comparable to the results of R M Patterson et al work, in which an exhaustive search was performed to find the farthest vertex within the bone mesh and whose distance was calculated as length [34]. The length of triquetrum was close to the measures obtained using a vinier caliper [38]. In addition, the surface area and volume had considerable variation between individuals with high standard deviations, indicating anatomical diversity within the population studied. The median values of scaphoid's surface area (1001,85 mm^2) and volume (2170,11 mm^3), trapezium's surface area (873,58) and volume (1847,51), and trapezoid's surface area (656,85) and volume (1237,57) were comparable with that of the values in literature [74].

The angle measures deviated to from that of the literature[40] which is the due to the approach taken to measure the same. This is mainly due to the reason on how the long axis of the bone is plotted and the angle measure in 3D rather in 2D. It also considerably varied from the approach in which the landmarks of required points were manually marked [65]. The carpal ratio measured in this study was observed to be higher than reported in literature, with the mean value being approximately one unit greater [39].

The joint surfaces were segmented using 2 approaches, and the measures extracted from the surfaces of these measures were shown to be significantly different by paired t-test. The method using vertex normal and proximity values for segmentation has a higher dependence on the thresholds provided during the segmentation process, as demonstrated in the study using the hamate hook as an example and how they varied between the selected threshold values from that of the study in which the distance threshold was smaller [74]. The ANRICP approach adds a degree of robustness to this challenge by incorporating a template-based and non-rigid registration. Among the carpal articular surfaces, both approaches showed that the capitate-hamate articular surface had the highest surface area, while the mean curvature of the hamate-lunate was the highest with both approaches and the least with the scaphoid-capitate. The scaphoid-capitate had a negative (-0.01) value for average mean curvature, indicating that the surface is mostly flat but slightly concave in nature. While the lunate-capitate articular surface also had a value (0.01) indicating that it is mostly flat but slightly convex in nature, these values were obtained using the NRICP method. Among the radial and ulnar articular surfaces, the radio-scaphoid articular surfaces had the lowest average mean curvature. Regarding the difference between males and females, females generally had a higher curvature value [75]. Understanding these variations among the population will play a critical role in the development of improved TWR implants, such as having the implants for women have a higher curvature characteristic to ensure a better fit to preserve the natural mobility of the patient's wrist.

To understand the natural grouping to provide a general requirement to design a series of TWR implants, a hierarchical clustering was performed as well as aid in identifying and defining distinct morphological subtypes within the population. This also avoids the need to develop a unique design for each patient, instead directly using the implant developed for the group to which the patient belongs and, if necessary, making minor modifications to the same, making the process faster and retaining greater natural biomechanics [76].

The groupings were performed a combination of parameters to also see the variation depending on a particular variable. Importance value-based selection of parameters on general produced 15 unique groups among the population. Considering the parameters directly related to the TWR implant such as PCR carpal parameters, radial parameters with the binary variable ulnar_var produced 14 parameters, and considering the same parameters with the binary variable gender produced 11 distinct groups. The groups had different mean values for the parameters between the ulnar_var and gender variables. The use of these groups with their parameter variations can help in the design of implants.

This study has some limitations. The data set may not be fully representative of the entire population. The OSCD data did not mention the ethnicity of the patient and therefore may not include the anatomical variation of the border population. Although age and sex were included in the dataset, physical activity level was not mentioned as it may influence the geometry of the bone[77].

The accuracy of the segmented articular surface depends on the effectiveness of the ANRICP algorithm [58]. Although ANRICP was considered for its accuracy, the segmentation is still affected by potential errors. This approach is also influenced by the accuracy of the initial articular surface segmented by a medical professional. It was assumed that the entire dataset has type 2 lunate (71% incidence rate) [78]. It is also assumed that the lunate articulates with the hamate and the disk (ulna) [79]. his procedure was applied to the MC's, radius and ulna as the amount of bone imaged depended on the CT machine. While the vertex-normal and proximity approaches also depended on the proximity threshold.

There is a possibility of errors induced in measurements due to the image processing techniques used. As the measurement process includes several steps, and each step has the potential to introduce errors. For example, identifying of the styloid tip of radius involves in identifying the vertex with the point with the maximum X value (based on the coordinate system of the bone) can vary depending on the anatomical variation of the radius bone among the population.

The future research should include a wider range of dataset that also takes ethnicity and level of activity (profession) into consideration. As it is seen that there is a significant variation between ethnic groups [12, 13]. Including datasets of subjects with pathological conditions and comparing them with healthy subjects to understand its impact of the bone anatomy may help in predicting a better fit implant design [80]. Exploring advanced segmentation algorithms to segment articular surfaces automatically and not have lesser dependency on threshold values of manual interventions. Using the techniques to segment the articular surface from high resolution MRI images result accurate articular surface segments [81]. Additionally using biomechanical models can be used to understand the effects of anatomical variation on joint function and understand how it differs between the groups identified to enhance the design requirements of the TWR implants.

The currently used TWR's perform a partial carpectomy [28] this directly affects the wrist range of motion, with decreased normal wrist FE and radial deviations [82]. This procedure reduces the complex multilayered wrist joint to a simple radio-carpal joint. It is also observed that the DCR and PCR show different types of motion, where the DCR rotates along with the wrist motion, but the PCR primarily flexes and extends [83] and the PCR kinematics may be affected by the anatomical variation [84]. The future study can investigate the possibility of incorporating certain characteristics of the mid-carpal biomechanics into the design to reduce the unnatural stress caused by the substitution [2] and help to preserve a higher degree of natural biomechanics, as this affects the carpal bone behavior due to altered load transmission [85].

5 Conclusion

This study successfully extracted and analyzed the 3D wrist bone features, providing insight into the presence of significant variations in wrist bone anatomy among the population and between the sexes. These observed variations emphasize the need for patient-specific design of TWR implants to accommodate the diversity of anatomical features. The anatomical features were extracted automatically with very minimum manual intervention. This is to overcome the reliability of an observer in identifying landmarks before measurements, and that involved with traditional 2D radiographic based measurements. In addition, the study demonstrated the impact of different methods used in the segmentation of articular surfaces, having significantly different measures.

Hierarchical clustering analysis revealed distinct morphological groups within the populations, providing a basis for designing a range of TWR implants tailored to each group. This may streamline the implant selection process, reduce the need for fully customized implants, and improve surgical outcomes by preserving the patient's natural wrist biomechanics. Future studies including a broader population sample and pathological wrist data could lead to the formation of enhanced clusters, ultimately contributing to the development of improved TWR implants.

6 REFERENCES

1. Reigstad, O., *Wrist arthroplasty: Bone fixation, clinical development and mid to long term results*. Acta Orthopaedica,, 2014. **85**: p. 1-53.
2. Clay B. Townsend, M., Joseph Paladino, BS, Asif M. Ilyas, MD, MBA, *The Evolution & Outcomes of Total Wrist Arthroplasty: Current Concepts*. SurgiColl, 2024. **2**(1).
3. Schmidt, D.m.I., *Total Wrist Replacement: State of the Art, Challenges and Pitfalls: A Comparative Review*. Archives of Clinical Trials, 2022. **2**(3): p. 1-18.
4. Zhu, X.M., et al., *A systematic review of outcomes of wrist arthrodesis and wrist arthroplasty in patients with rheumatoid arthritis*. J Hand Surg Eur Vol, 2021. **46**(3): p. 297-303.
5. Eschweiler, J., Jianzhang Li, Valentin Quack, Björn Rath, Alice Baroncini, Frank Hildebrand, and Filippo Migliorini., *Total Wrist Arthroplasty—A Systematic Review of the Outcome, and an Introduction of FreeMove—An Approach to Improve TWA*. Life 12, 2022. **3**.
6. Cyrus Tsun-Kit Lau, R.C.-W.W., Wai-Wang Chau , Michael Chu-Kay Mak, Wing-Lim Tse and Pak-Cheong Ho, *Complications following total wrist replacement: A single-center retrospective review*. Journal of Orthopaedics, Trauma and Rehabilitation, 2024: p. 1-9.
7. Robert Walker, M., John Reynolds, and Peter Evans, MD, PhD, *Total Wrist Arthroplasty*. Operative Techniques in Orthopaedics, 2022. **32**(1).
8. LoGiudice, A. and H. Awan, *Wrist Arthritis and Arthrodesis: Preserving Function, Minimizing Problems*. Hand Clin, 2023. **39**(3): p. 353-365.
9. Moore, D.C., et al., *A digital database of wrist bone anatomy and carpal kinematics*. J Biomech, 2007. **40**(11): p. 2537-42.
10. Bazira, P.J., *Surgical anatomy of the hand*. Surgery, 2022(40): p. 155-162.
11. C.E. Sulzmann, J.L.B., R.F. Pastor, *The utility of carpals for sex assessment: A preliminary study*. American Journal of Physical Anthropology, 2007. **135**(3): p. 252-262.
12. Mastrangelo, P., et al., *Sex assessment from the carpals bones: discriminant function analysis in a 20th century Spanish sample*. Forensic Sci Int, 2011. **206**(1-3): p. 216 e1-10.
13. Mastrangelo, P., S. De Luca, and G. Sanchez-Mejorada, *Sex assessment from carpals bones: discriminant function analysis in a contemporary Mexican sample*. Forensic Sci Int, 2011. **209**(1-3): p. 196 e1-15.
14. Kivell, T.L., I. Guimont, and C.E. Wall, *Sex-related shape dimorphism in the human radiocarpal and midcarpal joints*. Anat Rec (Hoboken), 2013. **296**(1): p. 19-30.
15. Eschweiler J, L.J., Quack V, Rath B, Baroncini A, Hildebrand F, Migliorini F, *Anatomy, Biomechanics, and Loads of the Wrist Joint*. Life (Basel), 2022. **12**(2): p. 188.
16. Yazaki, N., et al., *Variations of capitate morphology in the wrist*. J Hand Surg Am, 2008. **33**(5): p. 660-6.
17. Clitherow, H.M., Stuart & Fraysse, Francois & Costi, John & Eng, Kevin & Maguire, Duncan & Thewlis, Dominic, *The effect of lunate morphology on three-dimensional carpal kinematics*. The Journal Of Hand Surgery, 2014. **in-press**.
18. Berger, R.A., *The anatomy and basic biomechanics of the wrist joint*. J Hand Ther, 1996. **9**(2): p. 84-93.
19. Carolyn T. Wadsworth, M., LPT, *Clinical Anatomy and Mechanics of the Wrist and Hand*. Journal of Orthopaedic & Sports Physical Therapy, 1983. **4**(4): p. 206-216.
20. Sinan Seber, H.G., Abdurrahman Özçelik, zge Günal, Ruhi Aydin, Nusret Köse *A two-dimensional wrist model for carpal instability and force transmission*. Joint Diseases andRelated Surgery, 2008. **19**(3): p. 127-132.

21. Majima, M., et al., *Load transmission through the wrist in the extended position.* J Hand Surg Am, 2008. **33**(2): p. 182-8.
22. Wollstein, R., et al., *Midcarpal Structure Effect on Force Distribution through the Radiocarpal Joint.* J Wrist Surg, 2019. **8**(6): p. 477-481.
23. Rodriguez-Merchan, E.C., et al., *Total Wrist Arthrodesis: An Update on Indications, Technique and Outcomes.* Arch Bone Jt Surg, 2023. **11**(3): p. 144-153.
24. Jefferson Li, D.C.W., and Nathan A. Hoekzema, *Total Wrist Arthrodesis.* Operative Techniques in Orthopaedics, 2020. **30**(4): p. 100830.
25. Melamed, E., et al., *Trends in the Utilization of Total Wrist Arthroplasty versus Wrist Fusion for Treatment of Advanced Wrist Arthritis.* J Wrist Surg, 2016. **5**(3): p. 211-6.
26. C. Got, B.G.V., P. K. Mansuripur, P. M. Kane, A. P. C. Weiss and J. J. Crisco, *The effects of partial carpal fusions on wrist range of motion.* The Journal of Hand Surgery, 2016. **41E**(5): p. 479-483.
27. Alfred B. Swanson (MD), G.R.M., *Swanson™ Flexible Finger Joint Implant*, in *Stryker*. 2021.
28. *Universal 2 ™ Total Wrist Implant System*, in *Integra LifeSciences* 2009.
29. (MD), B.D.A., *FREEDOM Wrist Arthroplasty System*, in *Smith Nephew*. 2021.
30. Stryker. *ReMotion Total Wrist System*. Available from: https://www.stryker.com/us/en/trauma-and-extremities/products/remotion-total-wrist.html.
31. Ceri, N., et al., *The morphological and morphometric features of the scaphoid.* J Hand Surg Br, 2004. **29**(4): p. 393-8.
32. Viegas, S.F., et al., *Measurement of carpal bone geometry by computer analysis of three-dimensional CT images.* J Hand Surg Am, 1993. **18**(2): p. 341-9.
33. A. Elise Barnes, D.T.C., Scott E. Burnett & Pasuk Mahakkanukrauh, *Sex estimation from the carpal bones in a Thai population.* Australian Journal of

Forensic Sciences, 2019. **52**(6): p. 665-680.
34. R M Patterson, K.W.E., S F Viegas, W L Buford, *Carpal Bone Anatomy Measured by Computer Analysis of Threedimensional Reconstructions of Computed tomography Images* J Hand Surg Am, 1995. **20**(6): p. 923-929.
35. Gurusamy, K., et al., *A Study on Sexual Dimorphism of Adult Wet Scaphoid Specimens.* Cureus, 2022. **14**(2): p. e22263.
36. Trentadue, T.P., et al., *Morphology of the scaphotrapeziotrapezoid joint: A multi-domain statistical shape modeling approach.* J Orthop Res, 2024. **42**(11): p. 2562-2574.
37. Madala Venkateswara Rao, L.H., *Morphological and Morphometric Study of Scaphoid Bone in South Coastal Population.* Indian Journal of Anatomy, 2019. **8**(2): p. 101-106.
38. A. Balci, G.Y., S. Kendir, S.T. Karahan, N. Apaydin, *The morphologic and morphometric features of the triquetrumLes caractéristiques morphologiques et morphométriques du triquétrum.* Hand Surgery and Rehabilitation, 2023. **42**(1): p. 40-44.
39. G R Nattrass, G.J.K., R Y McMurtry, R F Brant, *An Alternative Method for Determination of the Carpal Height Ratiot.* The Journal of Bone and Joint Surgery, 1994. **76**(1): p. 88-94.
40. Bhat, A.K., et al., *Normative Data of Carpal Bone Measurements in the Sample Adult Indian Population.* Indian J Plast Surg, 2024. **57**(4): p. 278-286.
41. M. J. Rainbow, A.L.W., J. J. Crisco and S. W. Wolfe, *Functional kinematics of the wrist.* The Journal of Hand Surgery, 2016. **41E**(1): p. 7-21.
42. Patricia Gómez Barbero, P.R.V., Daniel Montaner Alonso, José L. Rodrigo Pérez, *Macroscopic and digital anthropometry of the human scaphoid: a comparative study.* Eur J Anat, 2021. **25**(5): p. 563-570.

43. Ikumi, A.Y., Y.; Eda, Y.; Ishii, T, *Computer-Aided Assessment of Three-Dimensional Standard Bone Morphology of the Distal Radius.* Diagnostics, 2022. **12**(12): p. 3212.
44. Li D, L.X., Hou Z and Pan F, *Measurement of bony anatomical parameters of the distal ulna based on healthy adult data: A cross-sectional study.* Sec. Orthopedic Surgery, 2023. **10**.
45. Robert M. J. Sippo, T.E.K.H., and Eero Waris, *Computer-based three-dimensional measurement of carpal alignment: measurement techniques and normal ranges.* Journal of Hand Surgery, 2021. **46**(10): p. 1064-1071.
46. Kocak, N.G.C.S.E.M., *Volumetric Analysis of Carpal Bones by Sex with 3D Slicer Software Program.* . Int. J. Morphol., 2024. **42**(4): p. 1005-1010.
47. Ten Berg, P.W., et al., *Estimating Scaphoid Lengths Using Anatomical Measurements in the Wrist.* J Hand Surg Am, 2016. **41**(9): p. e279-84.
48. Patil, A., et al., *The accuracy of statistical shape models in predicting bone shape: A systematic review.* Int J Med Robot, 2023. **19**(3): p. e2503.
49. Arabi, H. and H. Zaidi, *Comparison of atlas-based techniques for whole-body bone segmentation.* Med Image Anal, 2017. **36**: p. 98-112.
50. Khan, N., et al., *Statistical multi-level shape models for scalable modeling of multi-organ anatomies.* Front Bioeng Biotechnol, 2023. **11**: p. 1089113.
51. Xu, Y., et al., *A statistical shape and density model can accurately predict bone morphology and regional femoral bone mineral density variation in children.* Bone, 2025. **193**: p. 117419.
52. Asseln, M., et al., *Sex-Specific Size Analysis of Carpal Bones: Implications for Orthopedic Biomedical Device Design and Therapy Planning.* Life (Basel), 2024. **14**(1).
53. Dr. Magnús Kjartan Gíslason, D.D.H.N., Ebrahimi, Farzad, ed, *Finite Element Modelling of a Multi-Bone Joint: the Human Wrist.* InTech, 2012: p. 77-98.
54. Zhao, K., et al., *A technique for quantifying wrist motion using four-dimensional computed tomography: approach and validation.* J Biomech Eng, 2015. **137**(7): p. 0745011-5.
55. Lalone, E.A., et al., *Development of an image-based technique to examine joint congruency at the elbow.* Comput Methods Biomech Biomed Engin, 2013. **16**(3): p. 280-90.
56. Lenz, A.L., et al., *Statistical shape modeling of the talocrural joint using a hybrid multi-articulation joint approach.* Sci Rep, 2021. **11**(1): p. 7314.
57. Foumani, M., et al., *In-vivo dynamic and static three-dimensional joint space distance maps for assessment of cartilage thickness in the radiocarpal joint.* Clin Biomech (Bristol), 2013. **28**(2): p. 151-6.
58. Teule, E.H.S., et al., *Automatic analysis of the scapholunate distance using 4DCT imaging: normal values in the healthy wrist.* Clin Radiol, 2024. **79**(8): p. e1040-e1048.
59. Anand A Joshi, R.M.L., Ramsey D Badawi, Abhijit J Chaudhari, *Registration-based Bone Morphometry for Shape Analysis of the Bones of the Human Wrist.* IEEE Trans Med Imaging, 2016. **35**(2).
60. Tajdari, F., et al., *Feature Preserving Non-Rigid Iterative Weighted Closest Point and Semi-Curvature Registration.* IEEE Trans Image Process, 2022. **31**: p. 1841-1856.
61. Nandi, D., Ashour, A.S., Samanta, S., Chakraborty, S., Salem, M.A.M. and Dey, N, *Principal Component Analysis in Medical Image Processing: A Study.* International Journal of Image Mining, 2015. **1**(1): p. 45-65.
62. Eshak, G.A., H.M. Ahmed, and E.A. Abdel Gawad, *Gender determination from hand bones length and volume using multidetector computed tomography: a study in Egyptian people.* J Forensic Leg Med, 2011. **18**(6): p. 246-52.
63. Le Minor, J.M. and E. Rapp, *Relative weights of the human carpal bones: biological and functional interests.* Ann Anat, 2001. **183**(6): p. 537-43.

64. Akhbari, B., et al., *In vivo articular contact pattern of a total wrist arthroplasty design.* J Biomech, 2021. **121**: p. 110420.
65. Winter, R., et al., *An Evaluation of the Reliability of Manual Landmark Identification on 3D Segmented Wrists.* J Bone Joint Surg Am, 2024. **106**(4): p. 315-322.
66. Archana Singh, P.S., Rakesh Gupta, Arun Singh, *Morphometric Analysis of Distal End of Dry Human Radius in Northern India and Its Clinical Implications in Relation to Wrist Joint and Inferior Radioulnar Joint Arthroplasty: A Cross-sectional Study.* International Journal of Anatomy, Radiology and Surgery, 2024. **13**(2): p. A001-A007.
67. Archana Singh, P.S., Rakesh Gupta, Arun Singh, *Morphometric Analysis of Distal End of Dry Human Radius in Northern India and Its Clinical Implications in Relation to Wrist Joint and Inferior Radioulnar Joint Arthroplasty: A Cross-sectional Study.* International Journal of Anatomy, Radiology and Surgery, 2024. **13**(2): p. A001-A007.
68. Kox, L.S., et al., *Well-founded practice or personal preference: a comparison of established techniques for measuring ulnar variance in healthy children and adolescents.* Eur Radiol, 2020. **30**(1): p. 151-162.
69. Sharma, A., A. Kumar, and P. Singh, *Anatomical study of the distal end of cadaveric human ulnae: a clinical consideration for the management of distal radioulnar joint injuries.* Singapore Med J, 2011. **52**(9): p. 673-6.
70. Gupta, C.N., S; Kurian, Punnose; Kalthur, Sneha; Palimar, Vikram; D'Souza, Antony, *A Morphological and Morphometric Study of Distal End of Ulna with Its Clinical Implications.* Journal of Datta Meghe Institute of Medical Sciences University, 2019. **14**(4): p. 360-364.
71. Ozturk, B. and Y. Celik, *Dendrogram for Anthropometric and Biomechanical Variables Causing Foot Deformities by Using Hierarchical Cluster Analysis: A Cross-Sectional Study.* J Chiropr Med, 2022. **21**(2): p. 108-115.
72. Wakker, A.M., et al., *A novel method to perform morphological measurements on three-dimensional (3D) models of the calcaneus based on computed tomography (CT)-imaging.* Quant Imaging Med Surg, 2024. **14**(6): p. 3778-3788.
73. Zhang, Y., et al., *Comparison between three-dimensional CT and conventional radiography in proximal tibia morphology.* Medicine (Baltimore), 2018. **97**(30): p. e11632.
74. Taylor P. Trentadue, A.T., Cesar Lopez, Shuai Leng, David R. Holmes III, Sanjeev Kakar, Marco Rizzo, and Kristin D. Zhao, *Morphology of the scaphotrapeziotrapezoid joint: A multi-domain statistical shape modeling approach.* Journal of Orthopedic Research, 2024. **42**(11): p. 2562-2574.
75. Ateshian, G.A., M.P. Rosenwasser, and V.C. Mow, *Curvature characteristics and congruence of the thumb carpometacarpal joint: differences between female and male joints.* J Biomech, 1992. **25**(6): p. 591-607.
76. Honigmann, P., et al., *Patient-specific scaphoid prosthesis: surgical technique.* Arch Orthop Trauma Surg, 2024. **145**(1): p. 55.
77. Harding, A.T. and B.R. Beck, *Exercise, Osteoporosis, and Bone Geometry.* Sports (Basel), 2017. **5**(2).
78. Nakamura, K., et al., *Type I versus type II lunates: Ligament anatomy and presence of arthrosis.* J Hand Surg Am, 2001. **26**(3): p. 428-36.
79. D. Kamburov , G.M., S. Dyankova, *ANATOMICAL FEATURES OF OS LUNATUM: SIGNIFICANCE IN THE WRIST JOINT STATICS AND MECHANICS* Scripta Scientifica Medica, 1998. **30**: p. 49-55.
80. Bajuri, M.N., et al., *Biomechanical analysis of the wrist arthroplasty in rheumatoid arthritis: a finite element analysis.* Med Biol Eng Comput, 2013. **51**(1-2): p. 175-86.

81. Gu, H., et al., *SegmentAnyBone: A universal model that segments any bone at any location on MRI.* Med Image Anal, 2025. **101**: p. 103469.
82. Blankenhorn, B.D., et al., *Carpal kinematics after proximal row carpectomy.* J Hand Surg Am, 2007. **32**(1): p. 37-46.
83. Li, J., et al., *Wrist Bone Motion during Flexion-Extension and Radial-Ulnar Deviation: An MRI Study.* Life (Basel), 2022. **12**(10).
84. Norman, E., et al., *A Kinematic Analysis of Wrist and Carpal Function Using Four-Dimensional Computed Tomography Technology: A Dynamic Perspective.* J Hand Surg Am, 2025. **50**(3): p. 374 e1-374 e6.
85. Completo, A., et al., *Strain shielding in distal radius after wrist arthroplasty with a current generation implant: An in vitro analysis.* J Biomech, 2017. **52**: p. 169-175.

7 APPENDIX

7.1 APPENDIX A

7.1.1 A1

Complete Table of the articular surface measurments with the normal penetration concept.

Bone Name	Articular Surface	Parameter	Mean	SD	Bone name	Articular Surface	Parameter	Mean	SD
Capitate	Lunate	Length	11,95	1,39	Hamate	Capitate	Length	19,34	1,79
		Breadth	9,00	1,08			Breadth	12,80	1,39
		Surface_Area	93,87	20,46			Surface_Area	179,80	31,74
		Average_Mean_Curv	0,15	0,02			Average_Mean_Curv	0,08	0,01
		Average_Gaussian_Curv	5,95	0,62			Average_Gaussian_Curv	4,74	2,19
	Hamate	Length	20,37	1,90		MC4	Length	12,08	1,35
		Breadth	14,01	1,39			Breadth	9,50	1,44
		Surface_Area	190,48	33,27			Surface_Area	73,43	15,52
		Average_Mean_Curv	0,05	0,01			Average_Mean_Curv	0,08	0,02
		Average_Gaussian_Curv	4,72	0,46			Average_Gaussian_Curv	7,71	0,89
	Scaphoid	Length	15,25	2,12		MC5	Length	13,60	1,35
		Breadth	11,32	1,52			Breadth	9,65	1,30
		Surface_Area	142,11	29,43			Surface_Area	96,04	20,40
		Average_Mean_Curv	0,12	0,02			Average_Mean_Curv	0,06	0,01
		Average_Gaussian_Curv	5,21	0,67			Average_Gaussian_Curv	6,61	0,88
	Trapezoid	Length	14,93	1,93		Triquetrum	Length	14,78	2,04
		Breadth	11,35	1,82			Breadth	10,43	1,20
		Surface_Area	100,61	24,81			Surface_Area	115,15	26,15
		Average_Mean_Curv	0,09	0,03			Average_Mean_Curv	0,09	0,02
		Average_Gaussian_Curv	7,46	1,30			Average_Gaussian_Curv	5,65	0,58
	MC3	Length	15,53	1,66		Lunate	Length	8,65	2,02
		Breadth	11,63	1,43			Breadth	5,02	1,35
		Surface_Area	113,93	22,90			Surface_Area	24,63	11,78
		Average_Mean_Curv	0,09	0,01			Average_Mean_Curv	0,30	0,06
		Average_Gaussian_Curv	6,19	0,59			Average_Gaussian_Curv	14,26	4,86
Triquetrum	Hamate	Length	13,80	1,39	Trapezoid	Capitate	Length	15,28	1,56
		Breadth	11,91	1,29			Breadth	11,07	1,56
		Surface_Area	120,59	23,58			Surface_Area	112,90	21,34
		Average_Mean_Curv	0,07	0,02			Average_Mean_Curv	0,13	0,02
		Average_Gaussian_Curv	5,47	0,63			Average_Gaussian_Curv	5,95	0,62
	Lunate	Length	11,69	1,26		MC2	Length	15,90	1,44
		Breadth	10,00	1,19			Breadth	11,61	1,18
		Surface_Area	78,74	15,57			Surface_Area	138,13	24,59
		Average_Mean_Curv	0,12	0,02			Average_Mean_Curv	0,11	0,01
		Average_Gaussian_Curv	6,85	0,67			Average_Gaussian_Curv	5,23	0,45
	Pisiform	Length	9,30	1,37		Scaphoid	Length	11,94	2,05
		Breadth	7,73	1,27			Breadth	8,64	1,81

		Surface_Area	52,47	15,04
		Average_Mean_Curv	0,12	0,03
		Average_Gaussian_Curv	8,09	1,23
Scaphoid	Capitate	Length	17,46	1,55
		Breadth	12,85	1,26
		Surface_Area	170,37	29,38
		Average_Mean_Curv	0,05	0,01
		Average_Gaussian_Curv	4,60	0,50
	Lunate	Length	12,51	1,81
		Breadth	9,52	1,79
		Surface_Area	61,80	17,85
		Average_Mean_Curv	0,14	0,03
		Average_Gaussian_Curv	9,01	1,36
	Radius	Length	16,47	1,97
		Breadth	11,82	1,46
		Surface_Area	158,00	33,97
		Average_Mean_Curv	0,13	0,02
		Average_Gaussian_Curv	4,71	0,53
	Trapezoid	Length	11,59	2,18
		Breadth	7,66	1,67
		Surface_Area	56,71	17,43
		Average_Mean_Curv	0,14	0,03
		Average_Gaussian_Curv	8,44	1,20
	Trapezium	Length	12,12	1,52
		Breadth	8,99	1,32
		Surface_Area	81,61	19,79
		Average_Mean_Curv	0,12	0,02
		Average_Gaussian_Curv	6,69	0,83
Radius	Lunate	Length	17,71	1,89
		Breadth	13,31	1,98
		Surface_Area	171,26	42,43
		Average_Mean_Curv	0,03	0,02
		Average_Gaussian_Curv	4,95	1,08
	Scaphoid	Length	18,90	2,23
		Breadth	14,17	1,61
		Surface_Area	193,29	43,27
		Average_Mean_Curv	0,02	0,01
		Average_Gaussian_Curv	4,40	0,52
Ulna	Lunate	Length	9,007266	2,1022
		Breadth	5,63054	1,4986
		Surface_Area	33,36284	12,871
		Average_Mean_Curv	0,167094	0,0459
		Average_Gaussian_Curv	11,31234	3,6567

		Surface_Area	67,09	19,49
		Average_Mean_Curv	0,12	0,02
		Average_Gaussian_Curv	7,73	1,17
Lunate	Trapezium	Length	14,42	1,71
		Breadth	10,60	1,40
		Surface_Area	101,81	21,75
		Average_Mean_Curv	0,11	0,02
		Average_Gaussian_Curv	6,10	0,66
	Capitate	Length	15,16	1,44
		Breadth	10,08	1,52
		Surface_Area	122,51	25,56
		Average_Mean_Curv	0,06	0,01
		Average_Gaussian_Curv	5,49	0,57
	Radius	Length	15,24	1,72
		Breadth	11,69	1,69
		Surface_Area	133,95	34,59
		Average_Mean_Curv	0,13	0,01
		Average_Gaussian_Curv	5,45	1,14
	Scaphoid	Length	14,30	1,58
		Breadth	9,99	1,79
		Surface_Area	69,04	21,17
		Average_Mean_Curv	0,15	0,03
		Average_Gaussian_Curv	8,99	1,63
	Triquetrum	Length	11,56	1,38
		Breadth	10,44	1,36
		Surface_Area	74,84	15,84
		Average_Mean_Curv	0,09	0,02
		Average_Gaussian_Curv	7,25	0,67
	Ulna	Length	8,60	1,80
		Breadth	6,62	1,44
		Surface_Area	41,08	15,57
		Average_Mean_Curv	0,16	0,04
		Average_Gaussian_Curv	9,98	3,28
	Hamate	Length	11,93	2,70
		Breadth	7,40	2,01
		Surface_Area	36,90	16,10
		Average_Mean_Curv	0,15	0,06
		Average_Gaussian_Curv	13,65	4,31
MC3	Capitate	Length	15,69	1,61
		Breadth	12,19	1,43
		Surface_Area	121,35	23,35
		Average_Mean_Curv	0,11	0,01
		Average_Gaussian_Curv	5,91	0,57

MC1	Trapezium	Length	13,02	1,43	**MC4**	Hamate	Length	10,77	1,38
		Breadth	11,45	1,17			Breadth	8,36	1,38
		Surface_Area	118,90	23,90			Surface_Area	64,19	14,97
		Average_Mean_Curv	0,09	0,01			Average_Mean_Curv	0,18	0,03
		Average_Gaussian_Curv	5,39	0,53			Average_Gaussian_Curv	7,88	1,07
MC2	Trapezoid	Length	16,01	1,55	**MC5**	Hamate	Length	11,22	1,32
		Breadth	12,67	1,21			Breadth	9,96	1,18
		Surface_Area	147,40	26,24			Surface_Area	91,65	19,68
		Average_Mean_Curv	0,05	0,01			Average_Mean_Curv	0,14	0,02
		Average_Gaussian_Curv	5,14	0,52			Average_Gaussian_Curv	6,16	0,72
Trapezium	MC1	Length	14,40	1,51	**Pisiform**	Triquetrum	Length	9,26	1,34
		Breadth	10,31	1,55			Breadth	7,95	1,15
		Surface_Area	112,98	24,06			Surface_Area	57,18	15,08
		Average_Mean_Curv	0,09	0,01			Average_Mean_Curv	0,14	0,03
		Average_Gaussian_Curv	5,87	0,60			Average_Gaussian_Curv	7,42	1,07
	Scaphoid	Length	11,54	1,50					
		Breadth	9,83	1,36					
		Surface_Area	80,09	18,58					
		Average_Mean_Curv	0,11	0,02					
		Average_Gaussian_Curv	6,61	0,84					
	Trapezoid	Length	15,39	1,61					
		Breadth	10,87	1,33					
		Surface_Area	104,94	20,53					
		Average_Mean_Curv	0,08	0,01					
		Average_Gaussian_Curv	6,08	0,53					

7.1.2 A2

Complete Table of the articular surface measurments with the Amberg's Non-Rigid Transformation to tranform the segmented articulation surfaces from the source bone to target bones.

Bone Name	Articular Surface	Parameter	Mean	SD	Bone name	Articular Surface	Parameter	Mean	SD
		Length	9,75	0,82			Length	17,43	1,62
		Breadth	6,68	0,65			Breadth	12,34	1,17
	Lunate	Surface_Area	55,28	8,34		Capitate	Surface_Area	147,86	23,29
		Average_Mean_Curv	0,14	0,02			Average_Mean_Curv	0,06	0,01
		Average_Gaussian_Curv	8,21	0,58			Average_Gaussian_Curv	5,58	0,36
		Length	21,13	1,83			Length	7,22	0,58
		Breadth	11,62	1,00			Breadth	5,49	0,47
	Hamate	Surface_Area	176,85	29,16		MC4	Surface_Area	27,75	4,15
		Average_Mean_Curv	0,07	0,01			Average_Mean_Curv	0,00	0,05
		Average_Gaussian_Curv	5,64	0,37			Average_Gaussian_Curv	11,63	0,72
		Length	11,46	1,04			Length	10,39	0,90
		Breadth	9,36	0,73			Breadth	8,61	0,80
Capitate	Scaphoid	Surface_Area	86,23	13,30	**Hamate**	MC5	Surface_Area	69,35	11,83
		Average_Mean_Curv	0,13	0,02			Average_Mean_Curv	0,04	0,02
		Average_Gaussian_Curv	6,72	0,46			Average_Gaussian_Curv	7,73	0,55
		Length	14,26	1,41			Length	13,06	1,03
		Breadth	10,56	1,07			Breadth	9,45	0,79
	Trapezoid	Surface_Area	113,58	21,28		Triquetrum	Surface_Area	93,98	14,27
		Average_Mean_Curv	0,05	0,02			Average_Mean_Curv	0,10	0,02
		Average_Gaussian_Curv	6,70	0,55			Average_Gaussian_Curv	6,48	0,43
		Length	16,53	1,48			Length	8,52	0,70
		Breadth	10,09	1,06			Breadth	4,40	0,80
	MC3	Surface_Area	105,27	17,28		Lunate	Surface_Area	21,57	3,38
		Average_Mean_Curv	0,10	0,02			Average_Mean_Curv	0,27	0,04
		Average_Gaussian_Curv	7,06	0,43			Average_Gaussian_Curv	14,65	1,10
		Length	11,75	1,06			Length	15,14	1,38
		Breadth	8,19	0,72			Breadth	10,50	1,29
	Hamate	Surface_Area	68,07	11,10		Capitate	Surface_Area	117,45	20,93
		Average_Mean_Curv	0,02	0,02			Average_Mean_Curv	0,13	0,02
		Average_Gaussian_Curv	7,90	0,53			Average_Gaussian_Curv	6,29	0,53
		Length	10,82	0,96			Length	12,95	1,24
		Breadth	8,00	0,83			Breadth	9,77	0,98
Triquetrum	Lunate	Surface_Area	62,18	10,61		MC2	Surface_Area	93,27	15,65
		Average_Mean_Curv	0,09	0,02			Average_Mean_Curv	0,08	0,02
		Average_Gaussian_Curv	7,95	0,55	**Trapezoid**		Average_Gaussian_Curv	6,95	0,50
		Length	7,88	0,70			Length	11,68	1,19
		Breadth	5,97	0,59			Breadth	7,75	0,82
	Pisiform	Surface_Area	33,31	5,72		Scaphoid	Surface_Area	66,02	11,94
		Average_Mean_Curv	0,08	0,02			Average_Mean_Curv	0,14	0,02
		Average_Gaussian_Curv	10,61	0,87			Average_Gaussian_Curv	8,79	0,61
		Length	8,17	0,92			Length	12,35	1,14
		Breadth	6,69	0,69			Breadth	8,03	0,78
Pisiform	Triquetrum	Surface_Area	37,81	7,20		Trapezium	Surface_Area	69,03	12,06
		Average_Mean_Curv	0,10	0,04			Average_Mean_Curv	0,08	0,02
		Average_Gaussian_Curv	10,25	0,80			Average_Gaussian_Curv	7,89	0,59
		Length	13,23	1,33			Length	12,09	1,14
		Breadth	9,21	1,35			Breadth	8,89	0,91
	Capitate	Surface_Area	93,48	20,19		mc1	Surface_Area	79,16	14,18
		Average_Mean_Curv	0,01	0,02			Average_Mean_Curv	0,06	0,02
		Average_Gaussian_Curv	7,06	0,58			Average_Gaussian_Curv	7,86	0,55
Lunate		Length	13,82	1,36	**Trapezium**		Length	13,29	1,20
		Breadth	8,68	1,00			Breadth	9,03	0,88
	Radius	Surface_Area	93,48	18,83		Trapezoid	Surface_Area	79,50	14,13
		Average_Mean_Curv	0,13	0,01			Average_Mean_Curv	0,06	0,02
		Average_Gaussian_Curv	6,87	0,53			Average_Gaussian_Curv	7,51	0,47
	Scaphoid	Length	14,61	1,44		Scaphoid	Length	9,99	1,13
		Breadth	8,75	1,32			Breadth	9,07	0,94

		Surface_Area	61,22	12,47
		Average_Mean_Curv	0,10	0,03
		Average_Gaussian_Curv	9,81	0,72
	Triquetrum	Length	11,02	1,09
		Breadth	8,89	0,99
		Surface_Area	73,84	14,53
		Average_Mean_Curv	0,09	0,02
		Average_Gaussian_Curv	7,57	0,58
	Ulna	Length	8,51	0,83
		Breadth	5,67	0,58
		Surface_Area	38,64	7,05
		Average_Mean_Curv	0,13	0,02
		Average_Gaussian_Curv	10,09	0,74
	Hamate	Length	9,85	1,03
		Breadth	4,53	0,66
		Surface_Area	28,41	5,33
		Average_Mean_Curv	0,07	0,04
		Average_Gaussian_Curv	14,28	0,93

		Surface_Area	66,80	13,20
		Average_Mean_Curv	0,08	0,03
		Average_Gaussian_Curv	7,54	0,51
Scaphoid	Capitate	Length	12,77	1,30
		Breadth	11,46	1,18
		Surface_Area	111,39	19,26
		Average_Mean_Curv	-0,01	0,02
		Average_Gaussian_Curv	6,26	0,47
	Lunate	Length	10,74	1,01
		Breadth	7,39	0,83
		Surface_Area	54,46	10,10
		Average_Mean_Curv	0,15	0,03
		Average_Gaussian_Curv	9,18	0,74
	Radius	Length	14,60	1,40
		Breadth	11,18	1,08
		Surface_Area	115,91	20,80
		Average_Mean_Curv	0,13	0,01
		Average_Gaussian_Curv	6,36	0,48
	Trapezoid	Length	8,33	1,25
		Breadth	7,60	1,17
		Surface_Area	51,65	19,89
		Average_Mean_Curv	0,15	0,02
		Average_Gaussian_Curv	9,05	1,07
	Trapezium	Length	7,97	0,90
		Breadth	6,90	0,72
		Surface_Area	39,73	7,57
		Average_Mean_Curv	0,12	0,03
		Average_Gaussian_Curv	9,94	0,78

7.2 Appendix B

Box Plots of Articulation Curvatures

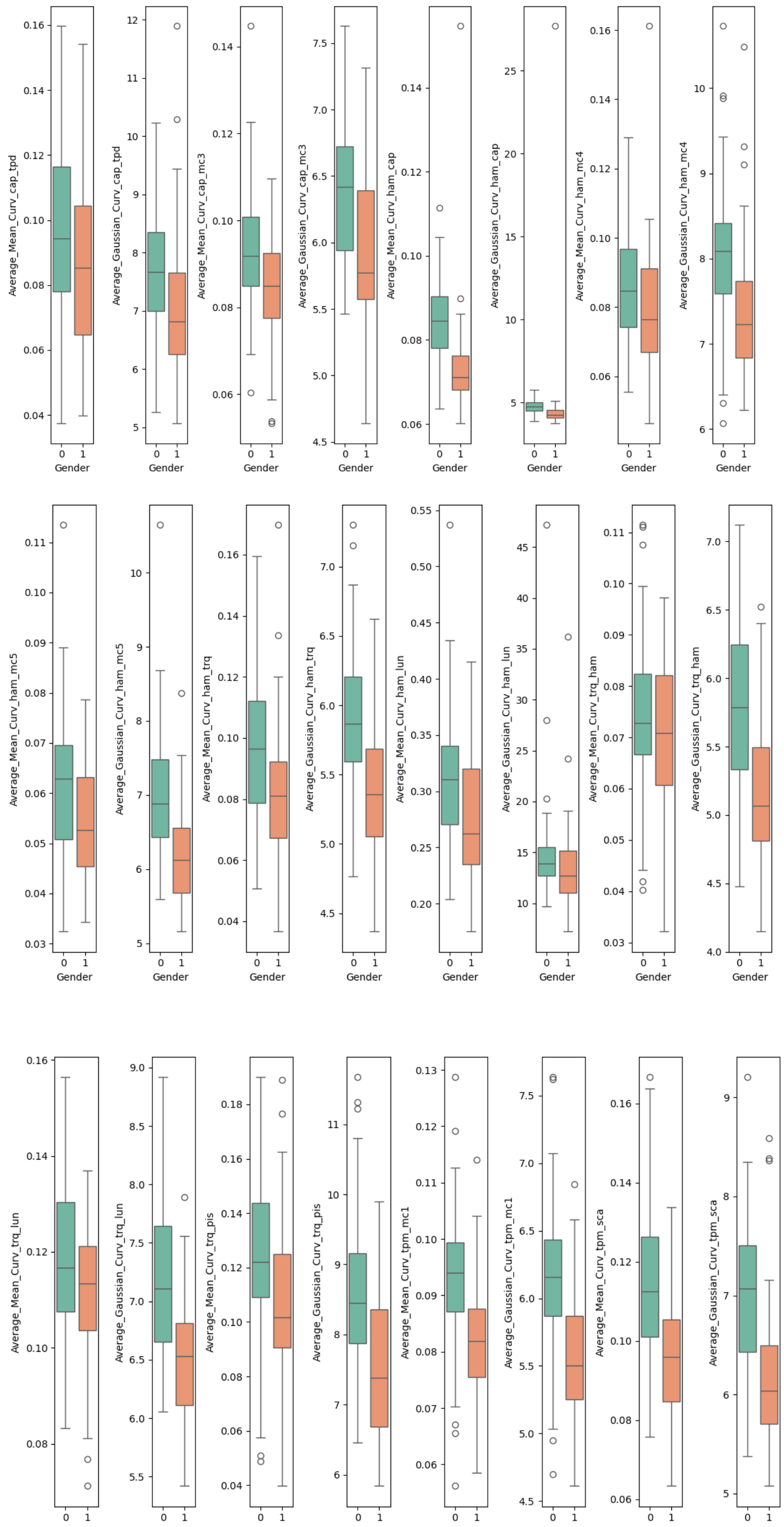

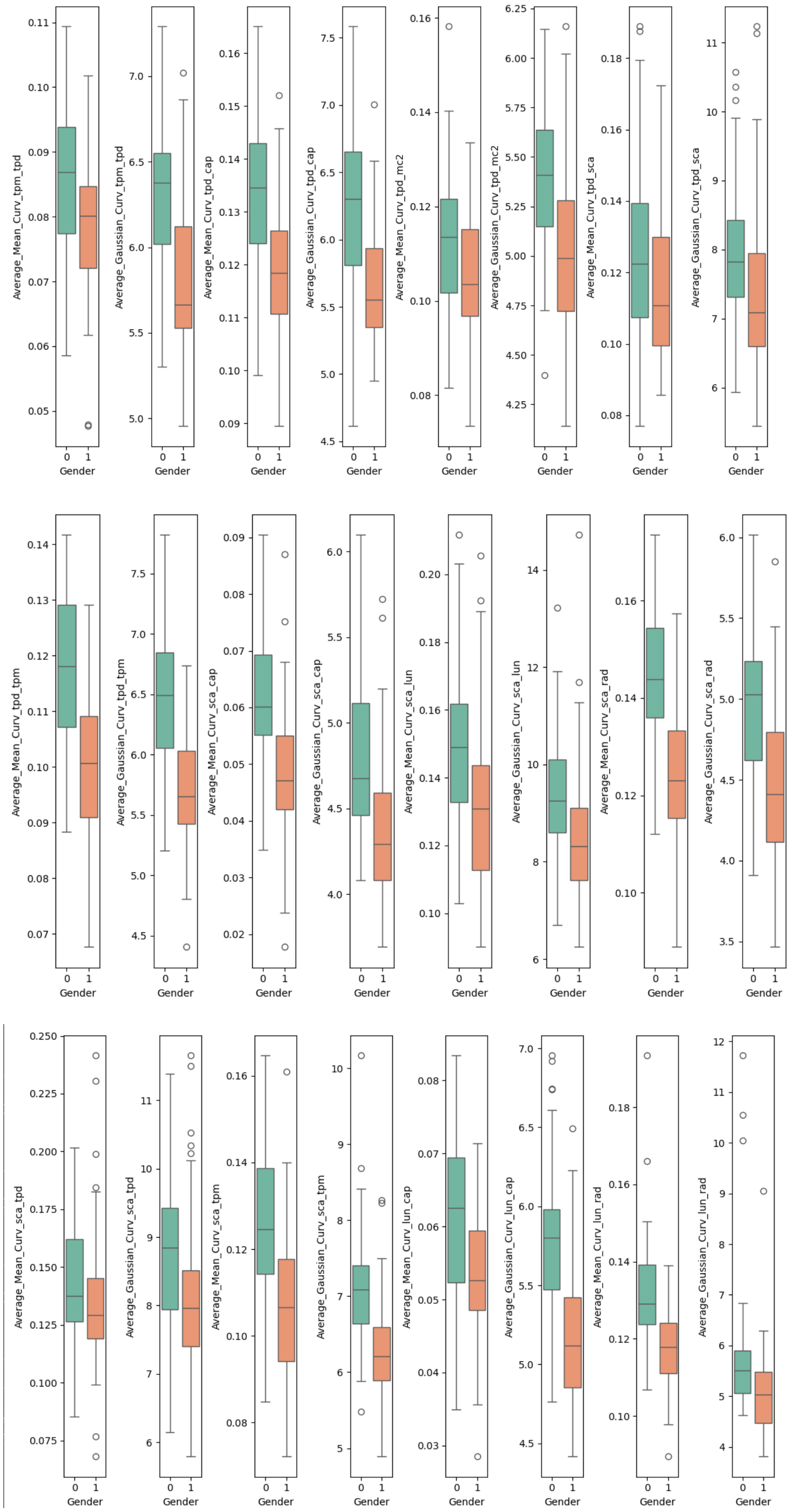
Average_Mean_Curv_tpm_tpd
Average_Gaussian_Curv_tpm_tpd
Average_Mean_Curv_tpd_cap
Average_Gaussian_Curv_tpd_cap
Average_Mean_Curv_tpd_mc2
Average_Gaussian_Curv_tpd_mc2
Average_Mean_Curv_tpd_sca
Average_Gaussian_Curv_tpd_sca
Average_Mean_Curv_tpd_tpm
Average_Gaussian_Curv_tpd_tpm
Average_Mean_Curv_sca_cap
Average_Gaussian_Curv_sca_cap
Average_Mean_Curv_sca_lun
Average_Gaussian_Curv_sca_lun
Average_Mean_Curv_sca_rad
Average_Gaussian_Curv_sca_rad
Average_Mean_Curv_sca_tpd
Average_Gaussian_Curv_sca_tpd
Average_Mean_Curv_sca_tpm
Average_Gaussian_Curv_sca_tpm
Average_Mean_Curv_lun_cap
Average_Gaussian_Curv_lun_cap
Average_Mean_Curv_lun_rad
Average_Gaussian_Curv_lun_rad
Gender

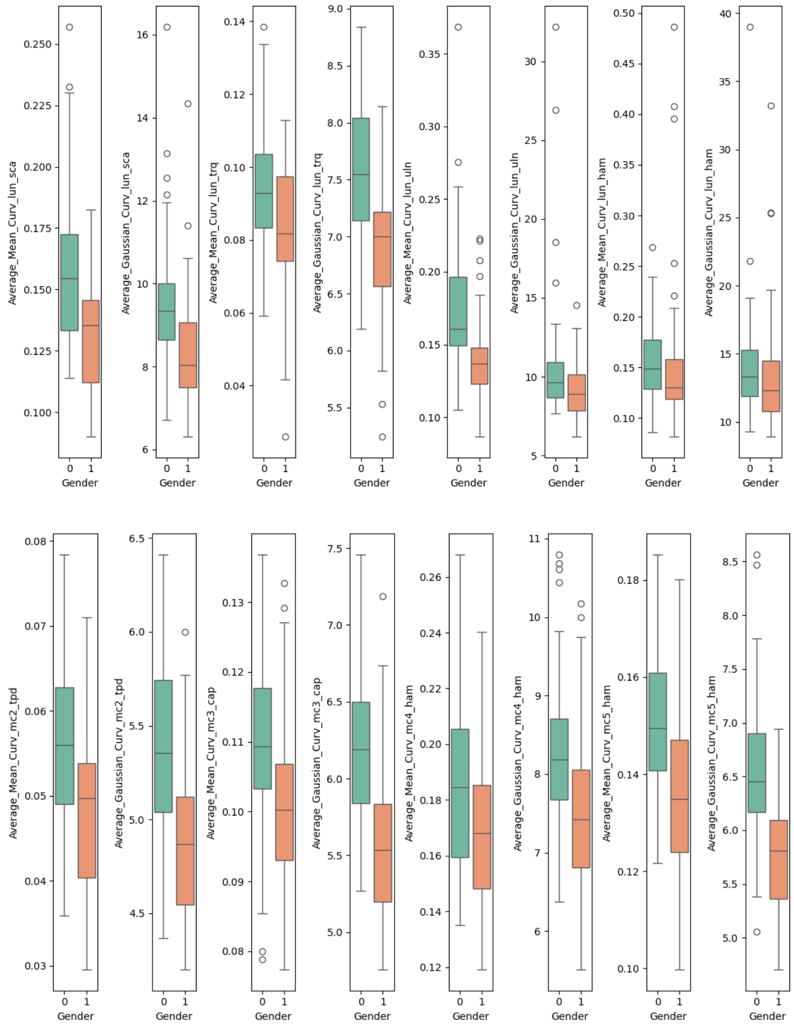
Average_Mean_Curv_lun_sca
Average_Gaussian_Curv_lun_sca
Average_Mean_Curv_lun_trq
Average_Gaussian_Curv_lun_trq
Average_Mean_Curv_lun_uln
Average_Gaussian_Curv_lun_uln
Average_Mean_Curv_lun_ham
Average_Gaussian_Curv_lun_ham
Average_Mean_Curv_mc2_tpd
Average_Gaussian_Curv_mc2_tpd
Average_Mean_Curv_mc3_cap
Average_Gaussian_Curv_mc3_cap
Average_Mean_Curv_mc4_ham
Average_Gaussian_Curv_mc4_ham
Average_Mean_Curv_mc5_ham
Average_Gaussian_Curv_mc5_ham
Gender

7.3 APPENDIX C

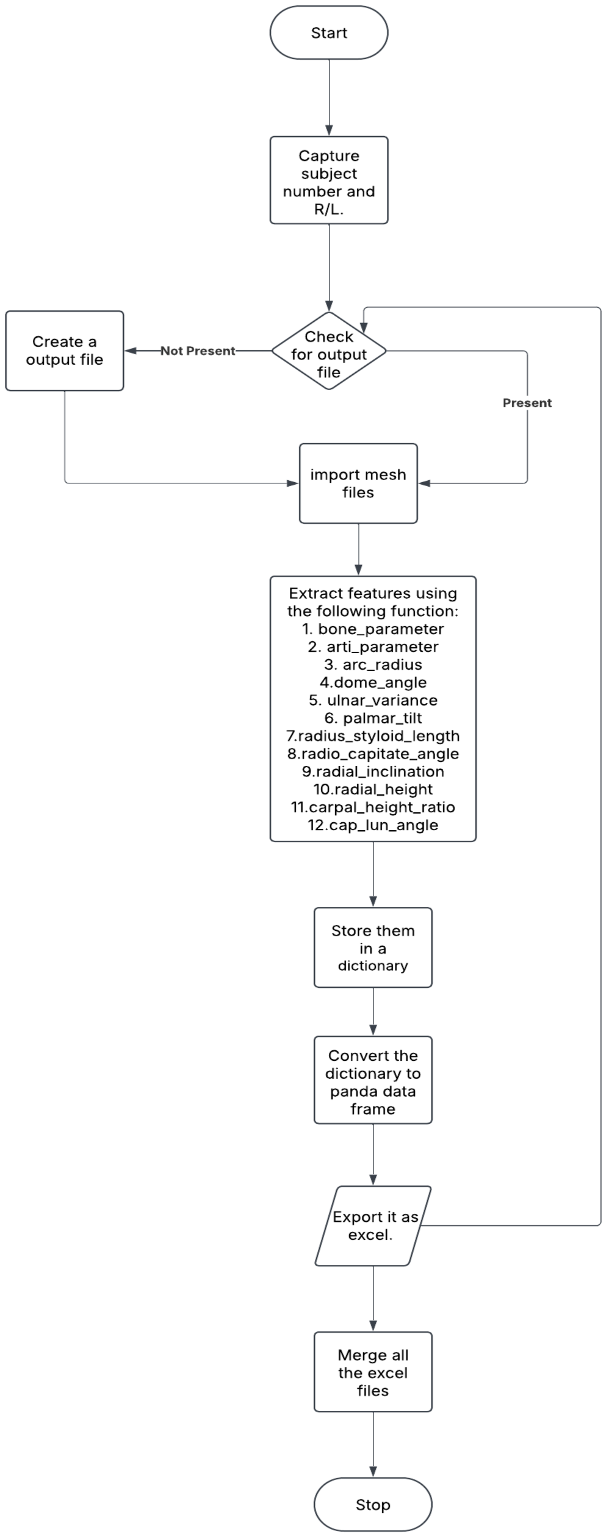

7.4 APPENDIX D